The Ly α, C iv, and He ii nebulae around J1000+0234: a galaxy pair at the centre of a galaxy overdensity at z=4.5

Jiménez-Andrade, E F; Cantalupo, S; Magnelli, B; Romano-Díaz, E; Gómez-Guijarro, C; Mackenzie, R; Smolčić, Vernesa; Murphy, E; Matthee, J; Toft, S

Source / Izvornik: **Monthly Notices of the Royal Astronomical Society, 2023, 521, 2326 - 2341**

Journal article, Published version
Rad u časopisu, Objavljena verzija rada (izdavačev PDF)

https://doi.org/10.1093/mnras/stad594

Permanent link / Trajna poveznica: https://urn.nsk.hr/urn:nbn:hr:217:142972

Monthly Notices of the ROYAL ASTRONOMICAL SOCIETY

MNRAS 521, 2326–2341 (2023)
Advance Access publication 2023 February 23

https://doi.org/10.1093/mnras/stad594

The Ly α, C IV, and He II nebulae around J1000+0234: a galaxy pair at the centre of a galaxy overdensity at $z = 4.5$

E. F. Jiménez-Andrade [1,2,3★] S. Cantalupo,[4★] B. Magnelli,[5] E. Romano-Díaz,[3] C. Gómez-Guijarro,[5] R. Mackenzie [6] V. Smolčić,[7] E. Murphy,[2] J. Matthee [6] and S. Toft[8,9]

[1]*Instituto de Radioastronomía y Astrofísica, Universidad Nacional Autónoma de México, Antigua Carretera a Pátzcuaro # 8701, Ex-Hda. San José de la Huerta, Morelia, Michoacán, C.P. 58089, México*
[2]*National Radio Astronomy Observatory, 520 Edgemont Road, Charlottesville, VA 22903, USA*
[3]*Argelander Institut für Astronomie, Universität Bonn, Auf dem Hügel 71, Bonn, D-53121, Germany*
[4]*Dipartimento di Fisica G. Occhialini, Università degli Studi di Milano Bicocca, Piazza della Scienza 3, I-20126 Milano, Italy*
[5]*Université Paris-Saclay, Université Paris Cité, CEA, CNRS, AIM, F-91191 Gif-sur-Yvette, France*
[6]*Department of Physics, ETH Zurich, Wolfgang-Pauli-Strasse 27, CH-8093 Zurich, Switzerland*
[7]*Department of Physics, Faculty of Science, University of Zagreb, Bijenička cesta 32, 10000 Zagreb, Croatia*
[8]*Cosmic Dawn Center (DAWN), DK-2800 Copenhagen, Denmark*
[9]*Niels Bohr Institute, University of Copenhagen, Jagtvej 128, DK-2200 Copenhagen, Denmark*

Accepted 2023 February 21. Received 2023 February 21; in original form 2022 October 14

ABSTRACT

Ly α λ1216 (Ly α) emission extending over $\gtrsim$ 10 kilo parsec (kpc) around dusty, massive starbursts at $z \gtrsim 3$ might represent a short-lived phase in the evolution of present-day, massive quiescent galaxies. To obtain empirical constraints on this emerging scenario, we present Ly α, C IVλ1550 (C IV), and He IIλ1640 (He II) observations taken with the Multi-Unit Spectroscopic Explorer towards J1000+0234: a galaxy pair at $z = 4.5$ composed of a low-mass starburst (J1000+0234−South) neighbouring a massive Submillimeter Galaxy (SMG; J1000+0234−North) that harbours a rotationally supported gas disc. Based on the spatial distribution and relative strength of Ly α, C IV, and He II, we find that star formation in J1000+0234−South and an active galactic nucleus in J1000+0234−North are dominant factors in driving the observed 40 kiloparsec-scale Ly α blob (LAB). We use the non-resonant He II line to infer kinematic information of the LAB. We find marginal evidence for two spatially and spectrally separated He II regions, which suggests that the two-peaked Ly α profile is mainly a result of two overlapping and likely interacting H I clouds. We also report the serendipitous identification of three Ly α emitters spanning over a redshift bin $\Delta z \leq 0.007$ (i.e. $\lesssim 380\,\mathrm{km\,s^{-1}}$) located at $\lesssim$ 140 kpc from J1000+0234. A galaxy overdensity analysis confirms that J1000+0234 lies near the centre of a Megaparsec-scale galaxy overdensity at $z = 4.5$ that might evolve into a galaxy cluster at $z = 0$. The properties of J1000+0234 and its large-scale environment strengthen the link between SMGs within LABs, tracing overdense regions, as the progenitors of local massive ellipticals in galaxy clusters.

Key words: galaxies: evolution – galaxies: high-redshift – galaxies: individual: J1000+0234 – galaxies: intergalactic medium.

1 INTRODUCTION

Extended nebulae of hydrogen Ly α λ1216 (Ly α) emission have become key observational signatures of high-redshift structures (see Ouchi, Ono & Shibuya 2020 for a review). The most extended with scale lengths $\gtrsim$ 100 kiloparsec (kpc) are associated with quasi-stellar objects (QSOs; e.g. Steidel et al. 2000; Cantalupo et al. 2014, 2019) and reside in overdense environments (e.g. Hennawi et al. 2015; Herenz, Hayes & Scarlata 2020; Li et al. 2021). The most compact nebulae, with scale lengths ranging from 1 to 20 kpc, have been found around star-forming galaxies (SFGs) at $z \approx 2-7$ via stacking (e.g. Steidel et al. 2011; Matsuda et al. 2012; Xue et al. 2017) and even direct detections (e.g. Wisotzki et al. 2016; Leclercq et al. 2017, 2020), suggesting that Ly α haloes (LAHs) are ubiquitous in high-redshift galaxies (Wisotzki et al. 2018). There is an intermediate population of Ly α nebulae with scale lengths of 10−100 kpc and Ly α luminosity of $\sim 10^{43}\,\mathrm{erg\,s^{-1}}$ that are usually labelled as Ly α blobs (LABs; e.g. Matsuda et al. 2004; Shibuya et al. 2018). These LABs are associated with a wide range of galaxy populations, including SFGs (e.g. Caminha et al. 2016; Geach et al. 2016), high-redshift radio galaxies (e.g. McCarthy et al. 1987; Swinbank et al. 2015; Marques-Chaves et al. 2019; Wang et al. 2021), quasars/QSOs (e.g. Borisova et al. 2016; Farina et al. 2017; Ginolfi et al. 2018; Travascio et al. 2020). LABs also tend to lie in galaxy overdensities (e.g. Matsuda et al. 2004; Erb, Bogosavljević & Steidel 2011; Alexander et al. 2016; Bădescu et al. 2017) and, as a result, these extended nebulae can be associated with multiple galaxies (Geach et al. 2014, 2016; Guaita et al. 2022; Solimano et al. 2022).

Particular emphasis is given to $z \gtrsim 3$ LABs surrounding dusty, highly active SFGs selected at sub-mm wavelengths, typically known

★ E-mail: e.jimenez@irya.unam.mx (EFJ-A); sebastiano.cantalupo@unimib.it (SC)

as Submillimetre Galaxies (SMGs; e.g. Geach et al. 2005, 2014, 2016; Hine et al. 2016; Guaita et al. 2022). The rare population of LABs around dusty galaxies with infrared luminosities $\log(L_{\rm IR}/{\rm L}_\odot) \gtrsim 12$ has an average source density of only $\sim 0.1\,{\rm deg}^{-2}$ (Bridge et al. 2013), likely because these systems undergo a short-lived, intense feedback phase that transforms high-redshift starbursts into mature/quenched systems (e.g. Bridge et al. 2013; Toft et al. 2014). LABs around luminous SMGs in rich environments might thus represent an early stage in the assembly of $z \gtrsim 2$ massive, quiescent galaxies (e.g. Gobat et al. 2012; Glazebrook et al. 2017) and local massive passive elliptical galaxies (e.g. Toft et al. 2014; Stach et al. 2021). To explore these scenarios, an accounting of energetic processes and environment around SMGs within LABs is needed. Nevertheless, information on the ionizing photon budget and overall kinematics of LABs is hampered by the resonant nature of Ly α line emission and, in the specific case of SMGs, dust absorption.

First, extended Ly α emission can be a result of resonant scattering of Ly α photons associated with star formation (e.g. Dijkstra & Loeb 2009a; Behrens & Braun 2014; Faucher-Giguère et al. 2015; Lake et al. 2015; Momose et al. 2016; Mas-Ribas et al. 2017), gravitational cooling radiation (e.g. Fardal et al. 2001; Dijkstra & Loeb 2009b), Ly α fluorescence, i.e. recombination radiation produced by gas photoionized by active galactic nuclei (AGNs) and/or cosmic ultraviolet (UV) background (e.g. Cantalupo 2017 for a review), and shock-heated gas by galactic superwinds (e.g. Taniguchi & Shioya 2000). Thus, complementary to Ly α observations, knowledge of other UV emission lines such as C IVλ1550 (C IV) and HeII λ1640 (He II) are necessary to infer better the physical processes powering Ly α emission (e.g. Villar-Martín, Tadhunter & Clark 1997; Villar-Martín et al. 2007; Cantalupo et al. 2019). The C IV/Ly α and He II/Ly α line ratios, in particular, can be compared with photoionization model predictions to disentangle the contribution of stellar-photoionized and AGN-ionized gas to the observed Ly α line emission (Villar-Martín et al. 2007; Arrigoni Battaia et al. 2015; Caminha et al. 2016; Cantalupo et al. 2019; Humphrey et al. 2019; Marques-Chaves et al. 2019; Herenz et al. 2020). Additionally, CIV line observations alone can inform about the distribution of metal-enriched gas in high-redshift nebulae (e.g. Marques-Chaves et al. 2019).

Secondly, despite the significant progress made to reproduce the observed Ly α properties of galaxies at high redshifts via radiative transfer modelling (e.g. Zheng et al. 2010; Sadoun et al. 2019; Song, Seon & Hwang 2020; Gurung-Lopez et al. 2021), kinematic information inferred from Ly α emission (e.g. Verhamme, Schaerer & Maselli 2006; Orsi, Lacey & Baugh 2012) is highly model dependant. Given the non-resonant nature of He II, this line arises as an unbiased probe of the gas kinematics (e.g. Cantalupo et al. 2019). Unfortunately, observations of the relative faint HeII and CIV lines in high-redshift galaxies are sparse (Prescott, Dey & Jannuzi 2009; Caminha et al. 2016), and have been preferentially detected in extreme environments around bright AGN/QSO (Dey et al. 2005; Cai et al. 2017; Cantalupo et al. 2019; Marino et al. 2019; Marques-Chaves et al. 2019; den Brok et al. 2020).

Here, we use the Multi-Unit Spectroscopic Explorer (MUSE) instrument to detect and characterize extended Ly α, CIV, and HeII emission around J1000+0234: a pair of galaxies at $z = 4.5$ constituted by an SFG with low stellar mass ($\log(M_\star/{\rm M}_\odot) = 9.2 \pm 0.1$) neighbouring a massive ($\log(M_\star/{\rm M}_\odot) = 10.1 \pm 0.1$) SMG (Gómez-Guijarro et al. 2018). We combine these observations with existing data from the Atacama Large Millimeter Array (ALMA) and *Hubble Space Telescope* (*HST*) to study the ionizing mechanisms, kinematics, and large-scale environment of the LAB around J1000+0234. We use this knowledge to evaluate evolutionary links between luminous SMGs in rich environments at $z > 3$, LABs, and quiescent systems in the centre of present-day galaxy clusters. This manuscript is organized as follows. The properties of J1000+0234 are given in Section 2. The details of the observations and data analysis are presented in Section 3, while the results are shown in Section 4. Finally, we discuss and summarize our main results in Section 5. Throughout, we assume a cosmology of $h_0 = 0.7$, $\Omega_M = 0.3$, and $\Omega_\Lambda = 0.7$.

2 J1000+0234

The system J1000+0234 was identified in the 1.1 mm map of the COSMOS field obtained with the AzTEC camera (Wilson et al. 2008) and the James Clerk Maxwell Telescope (Scott et al. 2008). J1000+0234 was subsequently associated with a Lyman Break Galaxy (LBG) using long-slit spectroscopy with the DEIMOS instrument at the Keck telescope, which revealed a prominent double-peaked Ly α line profile at $z = 4.547$ (Capak et al. 2008). ^{12}CO(2−1) and ^{12}CO(4−3) line observations unveiled a massive cold gas reservoir of $M_{\rm gas} \simeq 2.6 \times 10^{10} M_\odot$ (Schinnerer et al. 2008) in J1000+0234. Imaging with the *HST* and the Wide Field Camera 3 (WFC3), tracing the rest-frame UV emission, revealed that J1000+0234 is composed of two major – likely interacting – components separated by a projected distance of ≈ 6 kpc (see Fig. 1; Gómez-Guijarro et al. 2018). The northern and more massive component ($\log(M_\star/{\rm M}_\odot) = 10.1 \pm 0.1$; J1000+0234−North) is embedded in a dusty environment with $\log(L_{\rm IR}/{\rm L}_\odot) = 12.6 \pm 0.6$ and total star formation rate ${\rm SFR} = 500^{+1200}_{-320}\,{\rm M}_\odot\,{\rm yr}^{-1}$ (Gómez-Guijarro et al. 2018). A strong, double-peaked [C II] 158 μm emission line was detected with ALMA at the position of J1000+0234−North (at $z = 4.540$), indicating that this is a single, rapidly rotating disc with a dynamical mass of $\log(M_{\rm dyn}/{\rm M}_\odot) = 11.4-11.6$ (Jones et al. 2017; Fraternali et al. 2021).

The southern component, J1000+0234−South, has a stellar mass of $\log(M_\star/{\rm M}_\odot) = 9.2 \pm 0.1$, thus ∼10 times lower thanthat of J1000+0234−North. Yet, it emits the bulk of the rest-frame UV emission (75 per cent) observed with *HST*, consistent with the fact that no dust continuum (nor [CII] line) emission has been detected towards this component (Capak et al. 2008; Gómez-Guijarro et al. 2018). The UV emission indicates a ${\rm SFR} = 148 \pm 8\,M_\odot\,{\rm yr}^{-1}$ and a UV slope (β) of −2, as expected for LBGs at similar redshift (Gómez-Guijarro et al. 2018, and references therein). Finally, the SFR and stellar mass of J1000+0234−South and J1000+0234−North imply that these galaxies lie at 1.3 and 1.0 dex, respectively, above the main sequence of SFGs at $z = 4.5$ (assuming the relation from Schreiber et al. 2015). In other words, the SFRs of J1000+0234−North and J1000+0234−South are one order of magnitude higher than that of normal, main-sequence galaxies at the same redshift and stellar mass range. We, therefore, deem J1000+0234−South and J1000+0234−North as starburst galaxies.

3 MUSE OBSERVATIONS AND DATA ANALYSIS

3.1 Observational data and reduction

J1000+0234 has been observed with MUSE mounted on the Very Large Telescope (VLT-Yepun, UT4) using 16 exposures of 900 s and ground-layer adaptive optics. Each exposure was dithered slightly (randomly by ≈1–2 arcsec) and rotated by 90 deg compared to the previous exposure. These data were obtained over three observing blocks on 2019 March 7, April 8, and May 5, under good weather

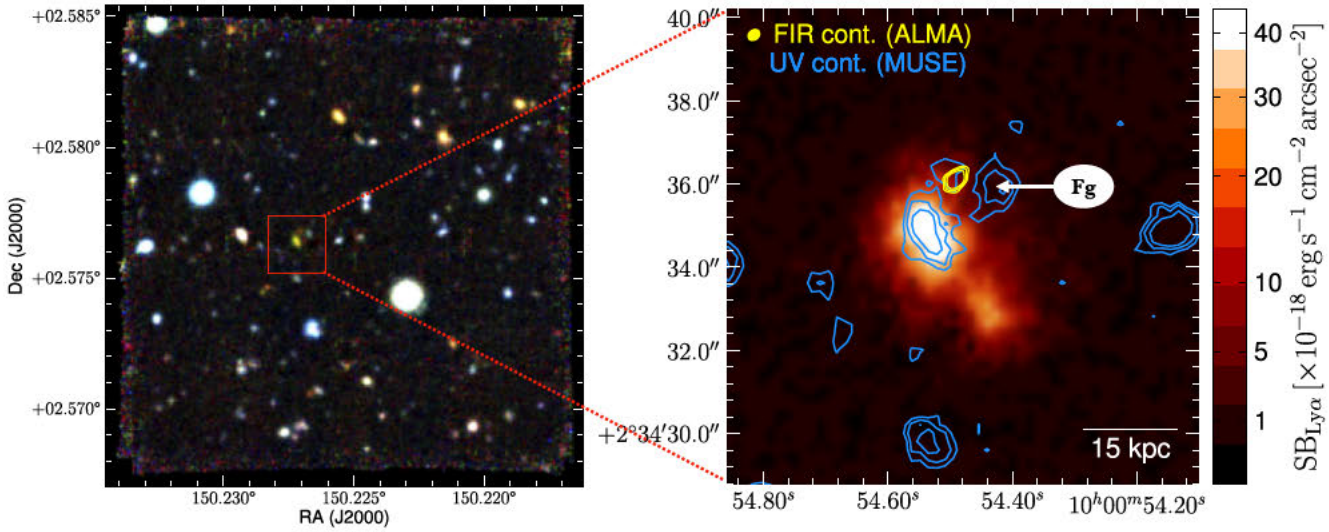

Figure 1. Left-hand panel: Three-colour image of the MUSE data cube obtained towards J1000+0234. The pseudo-bands used to create this RGB image have been defined as 'blue' (4875–6125Å), 'green' (6125–7375Å), and 'red' (7375–8625Å). The red square illustrates the zoomed-in region shown in the right panel, which displays the optimally extracted surface brightness (SB) maps of detected Ly α emission of J1000+0234. The blue contours show the rest-frame UV continuum emission detected by MUSE (at ∼1200 Å for $z = 4.5$), while the yellow contours illustrate the rest-frame far-infrared (FIR) continuum emission revealed by ALMA (at ∼ 160 μm for $z = 4.5$; Gómez-Guijarro et al. 2018). The ALMA beam shape is shown in the top-left corner. The UV and FIR emission contours are at 3, 5, and 8 times the rms noise level. The thin white contour indicates the SNR $= 3$ isophote of the Ly α SB map. The locus of the foreground 'Fg' galaxy ($z = 1.41$; Capak et al. 2008) exhibiting UV continuum emission is indicated by the white arrow.

conditions with an average seeing FWHM ≈ 0.9 arcsec and airmass <1.4. These observations, with a total integration time on source of 4 h, are part of the ESO GTO programmes 0102.A-0448 and 0103.A-0272 (PIs: S. Lilly and S. Cantalupo). The standard reduction steps (bias subtraction, flat-fielding, wavelength and flux calibration, geometrical cube reconstruction) are performed using the ESO MUSE pipeline (version 2.6; Weilbacher et al. 2014) without performing sky-subtraction. Then, we employ the CUBEXTRACTOR package [CUBEX hereafter, see Cantalupo et al. (2019) for a description] to improve flat-fielding and perform sky subtraction using CUBEFIX and CUBESHARP. Such an additional flat-fielding with CUBEFIX is implemented to reduce significant residuals in the white-light images generated by the pipeline (see section 2.1 of Cantalupo et al. 2019 for a detailed description of this step). We combine the individual exposures using CUBECOMBINE that applies an average-sigma clipping method. Half of the exposures were affected by intra-dome light contamination around 8000−9000 Å due to a malfunctioning monitoring camera.[1] Hence, we created two different data cubes with CUBECOMBINE. The first data cube only contains 'clean' exposures ('cleanexp' data cube hereafter) that account for 50 per cent of all the available data. It is, therefore, suitable for identifying C IV and He II at the expected observed wavelength of 8560 Å and 9086 Å, respectively. The second data sample, hereafter 'allexp' cube, contains all the exposures, regardless if they are affected or not by the issue mentioned above. The effective/clean spectral region of this data cube is 5000−8000 Å, allowing us to probe Ly α emission at the expected observed wavelength of 6742 Å. The 'cleanexp' and 'allexp' data cubes have a 1σ noise level of ≈2.0 and 1.4 $\times 10^{-20}$erg s^{-1} cm^{-2} arcsec^2, respectively, per layer (at 6650 Å) within an aperture of 1 arcsec^2. Both data cubes have a spectral resolution of 1.25 Å and pixel scale of 0.2 arcsec.

[1] https://www.eso.org/sci/facilities/paranal/instruments/muse/news.html; see the entry from 2019 May 31.

3.2 Continuum subtraction and three-dimensional signal extraction

The relative astrometry of MUSE data cubes is accurate (≈0.05 arcsec noise rms), yet the 'absolute' world coordinate system (WCS) can be off by a few arcsec. To calibrate the WCS of the 'allexp' and 'cleanexp' cubes, we use the position of bright point-like sources in the cubes and cross-match them with the coordinates inferred from *HST* imaging (Gómez-Guijarro et al. 2018), which was aligned to the absolute astrometry of the COSMOS field ensuring an absolute astrometric accuracy of ≈ 0.1 arcsec, or better, that is half of one pixel for our MUSE data cubes.

We use the routine CUBEBKGSUB from the CUBEX package to subtract the continuum of both cubes. We first mask the following spectral regions that exhibit evidence of line emission: 6725–6800Å (around Ly α), 8572–8612Å (around CIV), and 9071–9111Å (around He II). Then, we apply median filtering along the spectral axis using windows of 100 and 40 pixels for the Ly α, and C IV/He II spectral cube, respectively. We also smooth the resulting continuum across two neighbouring spectral bins.

A sub-cube that contains the spectral region around Ly α emission is extracted from the continuum-subtracted 'allexp' cube. This encompasses the layers/channels from 1580 to 1700, corresponding to the wavelength range of 6673.63–6823.63 Å. Similarly, two sub-cubes that cover the wavelength range around CIV (channels 3050–3180; 8510.8–8672.06 Å) and He II (channels 3495–3535; 9067.1–9117.1 Å) lines are extracted from the continuum-subtracted 'clean-exp' cube. We execute CUBEX on the subcube containing Ly α, line emission using the following configuration. We set `RescaleVar = true` to re-scale the original variance in the cube using the variance estimated layer by layer. We adopt `FilterXYRad = 2` to apply a Gaussian filter along the spatial direction using a 2-pixels radius. No Gaussian filter is applied along the wavelength direction (i.e. `FilterZrad = 0`). For the detection, we set a voxel individual threshold in signal-to-noise ratio (`SN-Thereshold`) of 2.5 and a minimum number of voxels (`MinNVox`) of 500. No

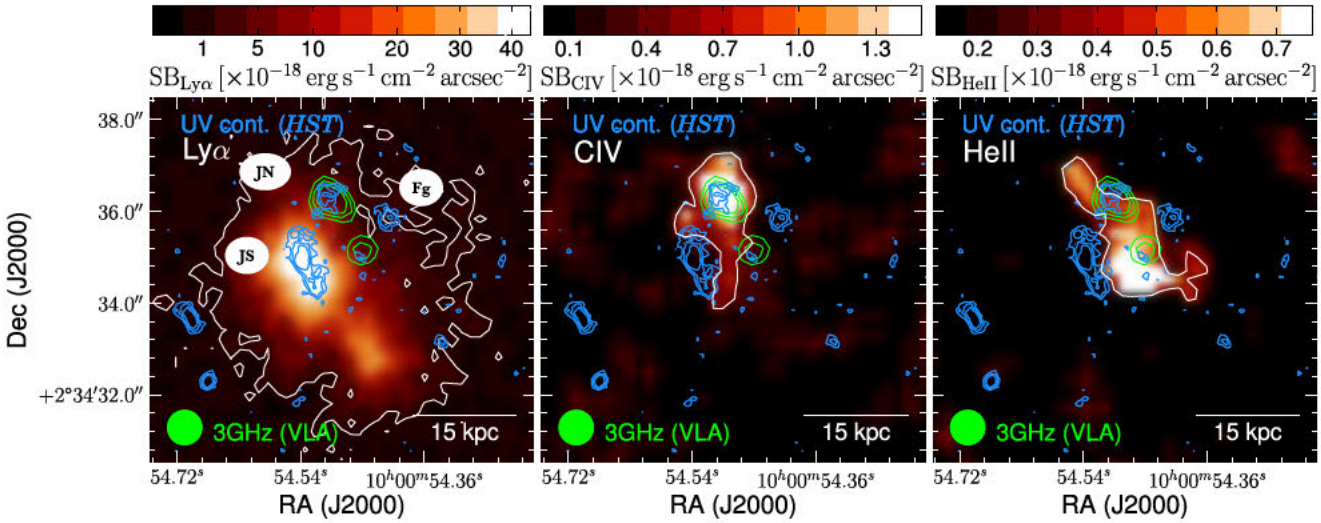

Figure 2. Optimally extracted SB maps of Ly α (left-hand panel), C IV (middle panel), and He II (right-hand panel) emission of J1000+0234. In the case of C IV and He II, we apply a spatial boxcar smoothing (2 × 2 pixels) to the cube before producing the SB maps (using the option `-boxsm` in CUBEX). The thin white contours indicate the SNR = 3 isophote. The blue contours show the rest-frame UV continuum from the *HST*/F160W imaging and the lime contours display the VLA 3 GHz radio continuum emission at 0.75 arcsec resolution (Smolčić et al. 2017b). The former are plotted at 3, 5, and 8 times the rms noise level, while the latter are drawn at 3, 4, and 5 times the rms noise level. The VLA beam shape is shown at the bottom-left corner. There are three prominent UV sources within the extended Ly α blob: a southern component associated with a low-mass SFG (J1000+0234−South: JS), a northern UV emitting source linked to a massive SMG (J1000+0234−North; JN) with a 3 GHz radio counterpart, and a foreground 'Fg' galaxy at $z = 1.41$ (Capak et al. 2008; Gómez-Guijarro et al. 2018). While the brightest Ly α region matches the locus of the low-mass SFG, the brightest C IV region is coincident with the SMG position. He II emission is maximal at ≈ 0.6 arcsec to the south-east of a compact 3 GHz radio source that has a faint UV counterpart.

minimum number of spatial/spectral pixels is adopted for detection (i.e. `MinArea` = 0 and `MinDz` = 0). We also mask the noisy edges of the data cube using `XYedges` = 30 pixels (6.2 arcsec). All the other parameters are set to the default values given by CUBEEX. Finally, to optimize the three-dimensional detection of the faint and compact C IV and He II emission, we run CUBEX using `MinNVox` = 100. The parameters `RescaleVar`, `FilterXYRad`, `FilterZrad`, `SNThereshold`, `MinArea`, and `MinDz` are set to the same values used to detect Ly α emission.

4 RESULTS

To explore the spatial distribution of the Ly α, C IV, and He II emission lines, we obtain surface brightness (SB) maps with the task `cube2im` (see Fig. 2). We use the IDCUBE inferred by CUBEX, while performing the 3D line extraction presented in Section 3.2. Such an `idcube` contains the three-dimensional masks associated with the source/line of interest. We also employ the task `cube2spc` to derive the 1D spectra of the Ly α, C IV, and He II emission lines (see Fig. 3). Because in deriving these 1D spectra we only consider the voxels in the three-dimensional masks, i.e. voxels with a sufficiently high signal-to-noise ratio (SNR > 2.5), we deem these spectra as 'optimally extracted'. The key properties of the Ly α, C IV, and He II emission lines reported in the CUBEX catalogues are presented in Table 1. These are discussed in more detail in the following paragraphs.

4.1 Ly α emission line

In the left-hand panel of Fig. 2, we overlay the rest-frame UV continuum emission from the *HST*/F160W imaging (with a $\approx 0\farcs2$ resolution; Gómez-Guijarro et al. 2018) over the velocity-integrated Ly α line emission map of J1000+0234. This overlay indicates that the brightest Ly α emitting region spatially correlates with the brightest UV component of the J1000+0234 complex. Interestingly, the rest-frame UV emission is elongated along the same direction of the Ly α nebula. This is further verified by the spatial distribution of the rest-frame UV continuum emission from the MUSE imaging (see the right-hand panel of Fig. 1). This UV-bright, low-mass SFG that we identify as JS (≡J1000+0234−South) appears to be linked to the ionizing source of the extended Ly α emission (see Section 5). Our extraction procedure with CUBEX indicates that such a Ly α nebula extends over a projected area of 42.9 arcsec^2 $\approx$ 1853 kpc^2. With an observed maximum linear projected size of $\approx$ 43 kpc, the emission around J1000+0234 appears to be among the most compact and faintest Ly α nebulae detected thus far if compared to nebulae detected around other AGN and bright quasars (Fig. 4). Since the observed total extent strongly depends on the detection limit, we note that the reported maximum linear size should be strictly interpreted as a lower limit to the full extent of the Ly α nebula. This lower limit, however, suffices to deduce that the Ly α nebula of J1000+0234 is brighter and larger than the typical Ly α haloes detected around galaxies (e.g. Leclercq et al. 2020).

The observed (optimally extracted) flux of $F^{\rm obs}_{{\rm Ly}\,\alpha} = 19.79 \pm 0.15 \times 10^{-17}$ erg s^{-1} cm^{-2} leads to a total line luminosity of $F^{\rm obs}_{{\rm Ly}\,\alpha} = 40.17 \pm 0.31 \times 10^{42}$ erg s^{-1}, assuming $z = 4.545 \pm 0.0002$ (see the following section), which sets J1000+0234 at the faint end of the luminosity distribution of Ly α nebulae around QSO, Type II AGNs, and high-redshift radio galaxies (Fig. 4). The 1D optimally extracted spectrum of J1000+0234 (the left-hand panel of Fig. 3) reveals a prominent emission line around 6750 Å associated with Ly α, which was originally reported by Capak et al. (2008). This broad and asymmetric line exhibits a double peak, suggesting complex gas kinematics in the Ly α nebula. We analyse and discuss the Ly α line profile in more detail in Section 5.2.

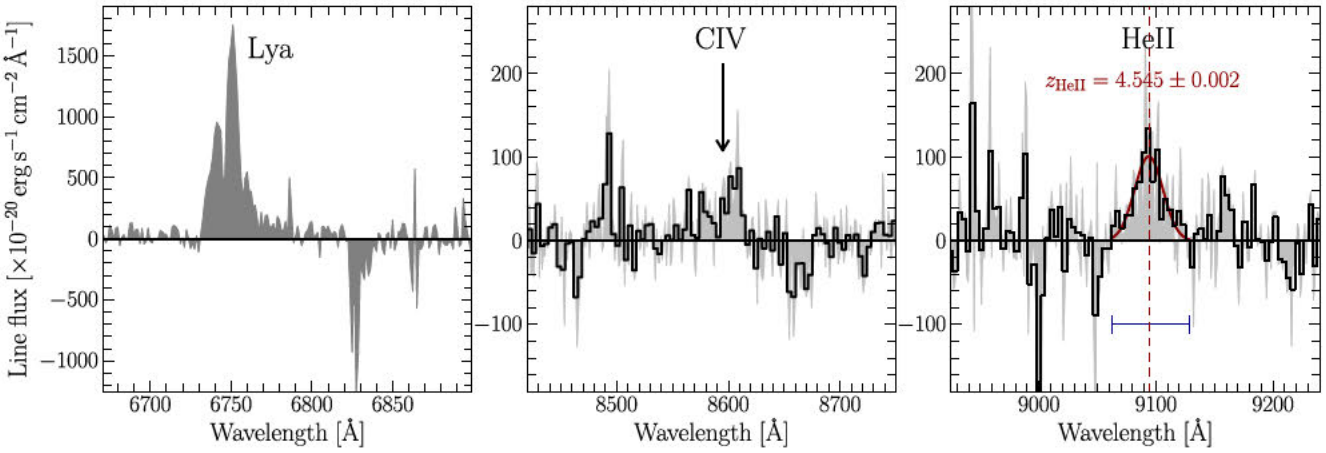

Figure 3. Optimally extracted 1D spectrum of the Ly α (left-hand panel), C IV (middle panel), and He II (right-hand panel) emission lines of J1000+0234. The solid histograms show the CIV and He II spectra averaged over a 4.5 Å-width bin. The strong negative features around 6830 Å are sky line residuals. The red line shows a Gaussian model to fit the He II line, and the vertical red-dashed line marks the central wavelength of the profile. The non-resonant HeII line indicates a redshift of 4.545 ± 0.002 for the J1000+0234 system. The horizontal bar shows the wavelength range used to fit the Gaussian model.

Table 1. Properties of Ly α, C IV, and He II emission lines of the full J1000+0234 system derived from our 3D line extraction procedure described in Section 4.

Emission line	RA (hh:mm:ss.sss)	Dec. (dd:mm:ss.ss)	Proj. area (arcsec^2 / kpc^2)	Iso flux ($\times 10^{-17}$erg s^{-1} cm^{-2})	Line luminosity ($\times 10^{42}$erg s^{-1})
Lyα	10:00:54.510	02:34:34.27	42.9/1853	19.79 ± 0.15	41.17 ± 0.31
CIV	10:00:54.509	02:34:35.94	3.7/159	0.37 ± 0.03	0.76 ± 0.07
HeII	10:00:54.478	02:34:35.18	5.5/238	0.27 ± 0.03	0.57 ± 0.06

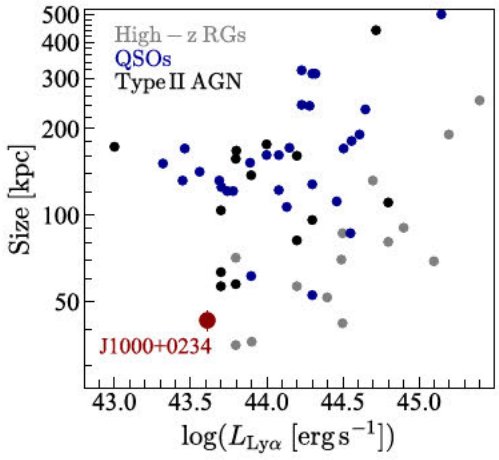

Figure 4. Total extent as a function of Ly α luminosity of LABs previously associated with high-redshift radio galaxies (High-z RGs), QSOs, and Type II AGN (using data from Marques-Chaves et al. 2019; Sanderson et al. 2021; Wang et al. 2021, and references therein). The total extent of the LABs around J1000+0234 is inferred using $\sqrt{a}$, where a is the projected area within which Ly α is significantly detected with CUBEX. The Ly α nebulae around the J1000+0234 system is among the most compact and dimmest LABs at $z \gtrsim 2$.

4.2 C IV and He II emission line

In the middle and right-hand panel of Fig. 2, we present the optimally extracted SB maps of CIV and HeII line emission. While CIV line emission peaks at the locus of J1000+0234−North (a massive, dusty starburst), the brightest HeII region encloses a faint UV continuum source that is offset by ≈1 arcsec to the west of the low-mass SFG J1000+0234−South. Such a faint source, originally identified by Gómez-Guijarro et al. (2018), is visible in the *HST*/F814W, *HST*/F125W, and *HST*/F160W imaging and has been labelled as a minor companion of the massive SMG J1000+0234−North (Gómez-Guijarro et al. 2018). There also exists a 3 GHz radio source detected at the 4.5σ level that lies at < 0.5 arcsec from this faint UV component and has a flux density of 1.0 ± 0.2 µJy (see our Fig. 2; Smolčić et al. 2017b).

Our source extraction procedure with CUBEX indicates that CIV and HeII emission extends out to a projected area of 3.7 arcsec^2 ≈ 159 kpc^2 and 5.5 arcsec^2 ≈ 238 kpc^2, respectively. With a total flux (i.e. flux of all voxels within the 3D detection mask) of $F^{\rm obs}_{\rm CIV} = 0.37 \pm 0.03 \times 10^{-17}$ erg s^{-1} cm^{-2} and $F^{\rm obs}_{\rm HeII} = 0.27 \pm 0.03 \times 10^{-17}$ erg s^{-1} cm^{-2}, we infer total line luminosities of $L_{\rm CIV} = 0.76 \pm 0.07 \times 10^{42}$ erg s^{-1} and $L_{\rm He\,II} = 0.57 \pm 0.06 \times 10^{42}$ erg s^{-1}(see Table 1). The optimally extracted spectra of the CIV and HeII emission lines are shown in the middle and right-hand panels of Fig. 3. Given the resonant nature of the Ly α and CIV emission lines, we use the He II line to infer the redshift of the J1000+0234 system. Fitting a 1D Gaussian model we find a central wavelength of 9093.8 ± 1.9Å (and FWHM = 12.1 ± 1.9 Å ≈ 940 ± 110 km s^{-1}), which implies a redshift of $z = 4.545 \pm 0.002$ that is comparable with that of J1000+0234−North (4.5391 ± 0.0004) derived from [CII] observations (Fraternali et al. 2021).

4.3 Large-scale environment of J1000+0234

The source extraction performed with CUBEXleads to the identification of five potential Ly α emitting sources within the 48.0 arcsec × 48.0 arcsec masked FoV (due to noisy edges) of MUSE (Fig. 5).

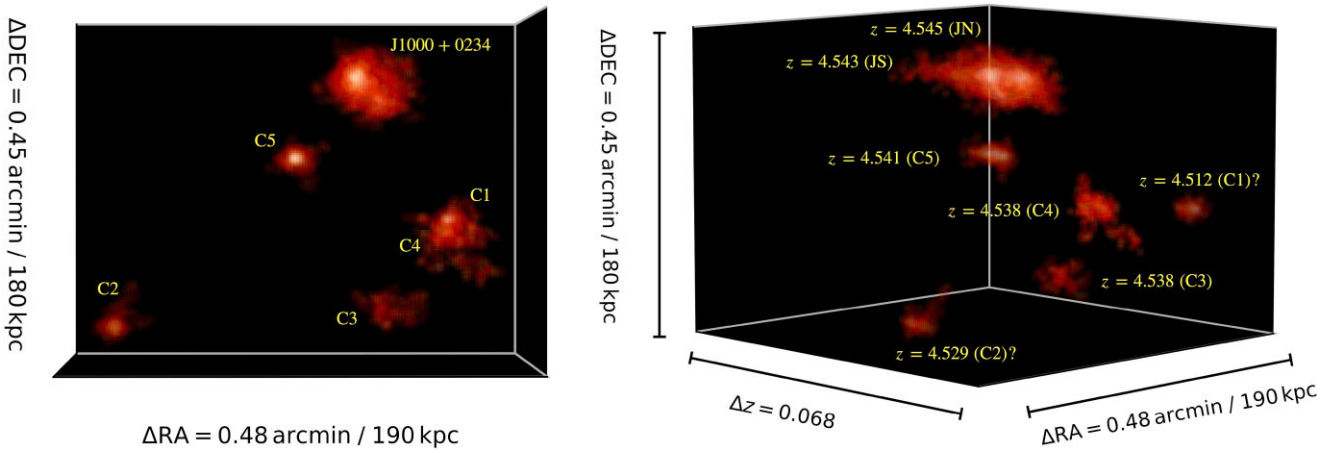

Figure 5. Ly α line emission of J1000+0234 and five emission-line sources (C1–C5) identified within a 48 × 48 arcsec^2 area around J1000+0234: as observed on the plane of the sky (left-hand panel) and along the wavelength/redshift axis (right-hand panel). The colour scale shows the flux density per voxel, normalized to the minimum and maximum value observed in this subcube. The redshift values presented for the five companions are derived under the assumption that the emission line corresponds to Ly α. The physical distance and redshift bins shown in the axis labels are computed at $z = 4.545$. The discovery of these companions around J1000+0234 support earlier results suggesting that this system resides in a galaxy overdensity, i.e. a protocluster, at $z = 4.5$ (Smolčić et al. 2017a).

The emission peaks of these sources are detected within a spectral window 6699.9–6743.6Å, implying a redshift offset $\delta z < 0.033$ (and velocity offset $\delta v < 1800\,\mathrm{km\,s^{-1}}$) with respect to J1000+0234. Extending the search for Ly α companions to larger spectral windows only reveals a detection of a potential Ly α emitter at $z = 4.428$, which is too distant ($\delta z = 0.117$, i.e. $\delta v \approx 6300\,\mathrm{km\,s^{-1}}$) from J1000+0234 to suggest membership. The optimally extracted SB maps of the five sources is presented in Fig. 6, while their optimally extracted 1D spectra and inferred line properties are shown in Fig. 7 and Table 2, respectively.

To verify that the observed line emission from the five neighbouring sources around J1000+0234 corresponds to Ly α at $z \approx 4.5$, we identify their UV counterparts in the *HST*/WFC3 continuum imaging (Gómez-Guijarro et al. 2018) and cross-match their positions with the CLASSIC COSMOS2020 photometric catalogue (Weaver et al. 2021). Using a 1.″0 search radius, we find the following:

(i) The two UV sources near the brightest emitting region of C5 are linked to a COSMOS2020 source with photometric redshift $z_p = 4.594 \pm 0.050$, $\log(M_\star/\mathrm{M}_\odot) = 10.24^{+0.10}_{-0.13}$, and SFR = $56^{+19}_{-11}\,\mathrm{M}_\odot\,\mathrm{yr}^{-1}$.

(ii) The central UV source in C4 has a photometric redshift $z_p = 4.505^{+0.330}_{-0.280}$, $\log(M_\star/\mathrm{M}_\odot) = 8.62^{+0.18}_{-0.22}$ and SFR = $2.0^{+2.7}_{-0.5}\,\mathrm{M}_\odot\,\mathrm{yr}^{-1}$. The UV source at the south-west of the central region of C4 is a foreground galaxy at $z_p = 1.623^{+0.470}_{-0.290}$.

(iii) The more compact UV source in C3 lies at $z = 4.608^{+0.190}_{-0.170}$, it has a stellar mass $\log(M_\star/\mathrm{M}_\odot) = 9.79^{+0.15}_{-0.23}$, and SFR = $25^{+44}_{-6}\,\mathrm{M}_\odot\,\mathrm{yr}^{-1}$. The more extended UV source is a foreground galaxy at $z = 0.892^{+0.050}_{-0.040}$.

(iv) The central UV source in C2 has a photometric redshift of $z_p = 0.781 \pm 0.050$, $\log(M_\star/\mathrm{M}_\odot) = 8.05 \pm 0.09$, and SFR = $0.28^{+0.10}_{-0.12}\,\mathrm{M}_\odot\,\mathrm{yr}^{-1}$. Based on this redshift estimate, the emission line of C2 at 6721.8 Å could correspond to the [OII] λ3727 doublet at $z = 0.803 \pm 0.001$. Indeed, the inferred [OII]-based SFR (Kennicutt 1998) of $0.35 \pm 0.10\,M_\odot\,\mathrm{yr}^{-1}$matches that reported in the CLASSIC COSMOS2020 catalogue. Assuming $z = 0.803 \pm 0.001$, the rest-frame separation between the peaks would be ≈3Å, which agrees with that of the [OII] λ3727 doublet. In addition, the symmetric double-peaked line at 6721.8 Å would be at odds with the typical Ly α line profiles of high-redshift galaxies where the blue peak can be significantly absorbed by the foreground intergalactic medium (e.g. Laursen, Sommer-Larsen & Razoumov 2011; Hayes et al. 2021), although prominent blue peaks due to gas accretion are expected as well (Ao et al. 2020). Since no other emission line is robustly detected at the locus of C2 in the MUSE data cube, we cannot firmly associate the 6721.8 Å line with [OII] λ3727 and confirm that C2 lies at $z \approx 0.8$. Given the ambiguity in the nature of the 6721.8 Å line, we do not rule out C2 as a likely Ly α companion around J1000+0234.

(v) No UV continuum counterpart is identified for C1. We deem this source as another potential Ly α emitter at $z = 4.512$.

In summary, the photometric redshifts of the UV counterparts of the extended C3, C4, and C5 sources support our initial assumption that their emission lines at ≈6735 Å correspond to Ly α. Focusing on these three – robustly identified – companions around J1000+0234, we observe that their Ly α luminosity ranges from 1.8 to $3.6 \times 10^{42}\,\mathrm{erg\,s^{-1}}$. Interestingly, the luminosity of these sources and their redshift/velocity offset with respect to J1000+0234 are anticorrelated (Table 2), i.e. the more luminous companions are closer (both on the plane of the sky and along the line of sight) to J1000+0234. The nearest companion, C5, lies at a projected distance of ≈50 kpc to the south-east of J1000+0234, while the farthest one (C3) lies at ≈140 kpc to the South of J1000+0234. Whereas Ly α emission in C5 is concentrated in a single component with a projected area of 315−460 kpc^2, the Ly α emission of C3 and C4 displays an extended, clumpy morphology that spreads out to a projected distance of 600 and 1090 kpc^2, respectively.

4.3.1 A galaxy overdensity around J1000+0234

Using the COSMOS2015 photometric catalogue (Laigle et al. 2016), Smolčić et al. (2017a) anticipated that J1000+0234 belongs to a galaxy overdensity. This result is reinforced by the discovery of Ly α emitters at $z \approx 4.5$ in the 317×317 kpc^2 (unflagged) FoV of our MUSE data cube. Here, we verify the overdensity by repeating the analysis presented by Smolčić et al. (2017a) using the new COSMOS2020 photometric redshift catalogue (Weaver et al. 2021) and the Ly α-detected sources in this work.

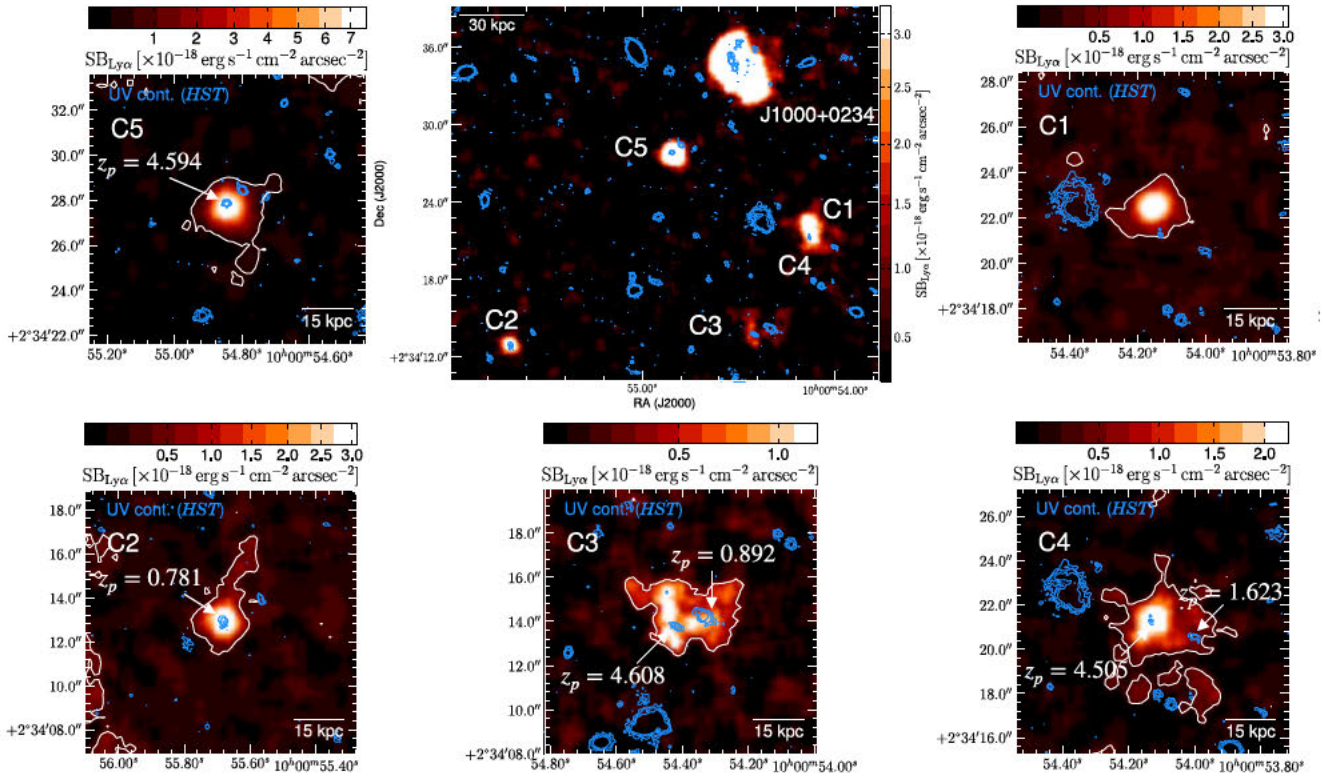

Figure 6. Spatial distribution (central panel) and optimally extracted SB maps (lateral/lower panels) of the five emission-line sources in the vicinity of J1000+0234. The blue contours show the rest-frame UV continuum from the *HST*/F160W imaging and are plotted at 3, 5, and 8 times the rms noise level. The photometric redshifts (if available) of the UV continuum sources located within the extended emission-line regions are shown in white. The UV counterparts of C3, C4, and C5 have a photometric redshift of $z_p \approx 4.5$. Therefore, we can robustly associate the C3, C4, and C5 emission-line regions with Ly α. Because there is no UV counterpart for C1 and because C2 might correspond to the [OII] λ3727 doublet of a $z = 0.803 \pm 0.001$ foreground galaxy, we deem C1 and C2 as potential Ly α emitting sources at $z \approx 4.5$.

For this analysis, we restrict the COSMOS2020 CLASSIC catalogue to (Subaru Suprime-Cam) sources with $i \leq 27.03$ to match the magnitude limit to our faintest MUSE source. The selected sources lie within the Ultravista area (FLAG_UVISTA = 0) and fall within the redshift range of $\Delta z = 0.53$ centred at the redshift of J1000+0234. No sources in the photometrically flagged areas in the Subaru Suprime-Cam data (FLAG_SUPCAM = 0) are considered. The above criteria select J1000+0234−North, J1000+0234−South, and their three robustly identified companions (C3, C4, and C5) from the COSMOS2020 catalogue.

We first run the Voronoi tessellation analysis which identifies overdensities by partitioning a plane into convex polygons called Voronoi cells. Each cell encloses exactly one point (in our case one galaxy in the chosen Δz range). The inverse of the volume of a galaxy's cell effectively corresponds to the local number density of galaxies for the given galaxy. The threshold above which a cell is considered 'overdense' was chosen to be the 80 per cent quantile of the cumulative distribution of cell densities obtained using 10 Mock catalogues. The Mock catalogues were generated to contain the same number of galaxies as present in the inner 1 deg^2 of the COSMOS field, but with randomly distributed positions over this area. For more details about the method, see section 3.1.2 in Smolčić et al. (2017a). The Voronoi tessellation analysis results are presented in the left-hand panel of Fig. 8, where we indicate only galaxies occupying 'overdense' cells. An overdensity, centred on the four sources, J1000+0234, C3, and C5, is clearly discernible.

We further compute the galaxy overdensity parameter (δ_g) as a function of distance from the identified centre of the overdensity that is RA = 150.22578 deg and Dec. = 2.572560 deg. This is done by equalling the overdensity centre to the average right ascension and declination of sources within the red circle in the left-hand panel of Fig. 8 (see section 3.1 in Smolčić et al. 2017a for more details). The galaxy overdensity parameter, which is the contrast above the background field, is defined as a function of radius (r):

$$\delta_g(r) \equiv \frac{\Sigma_r(r) - \Sigma_{bg}}{\Sigma_{bg}} = \frac{\Sigma_r(r)}{\Sigma_{bg}} - 1\,, \quad (1)$$

where Σ_r and Σ_{bg} are the local galaxy, and the background galaxy surface density, respectively. The overdensity parameter then equals zero, $\delta_g = 0$ (i.e. $\Delta\Sigma = 0$), for no observed overdensity, $\delta_g > 0$ indicates an overdensity, while $\delta_g < 0$ indicates an underdensity.

The average value of the background surface density (Σ_{bg}) was computed using nine differently positioned, circular, and not overlapping $A_{bg} = 706.86$ arcmin^2 areas. Errors, reflecting statistical fluctuations, were then assigned on $\delta_g(r) = 0$, i.e. $\sigma_{\delta_g=0}(r)$ (see section 3.1.3 in Smolčić et al. 2017a for more details).

The results are shown in the right-hand panel of Fig. 8, where we show δ_g as a function of radius, computed in steps of 0.1 arcmin, as well as the signal-to-noise ratio, $\delta_g/\sigma_{\delta_g}$. We also indicate δ_g values for which the Poisson probability of observing more or equal number of sources than expected from the background galaxy surface density is $\leq$0.05, considering these to be robust overdensity values. As seen in Fig. 8, a galaxy overdensity is detected out to

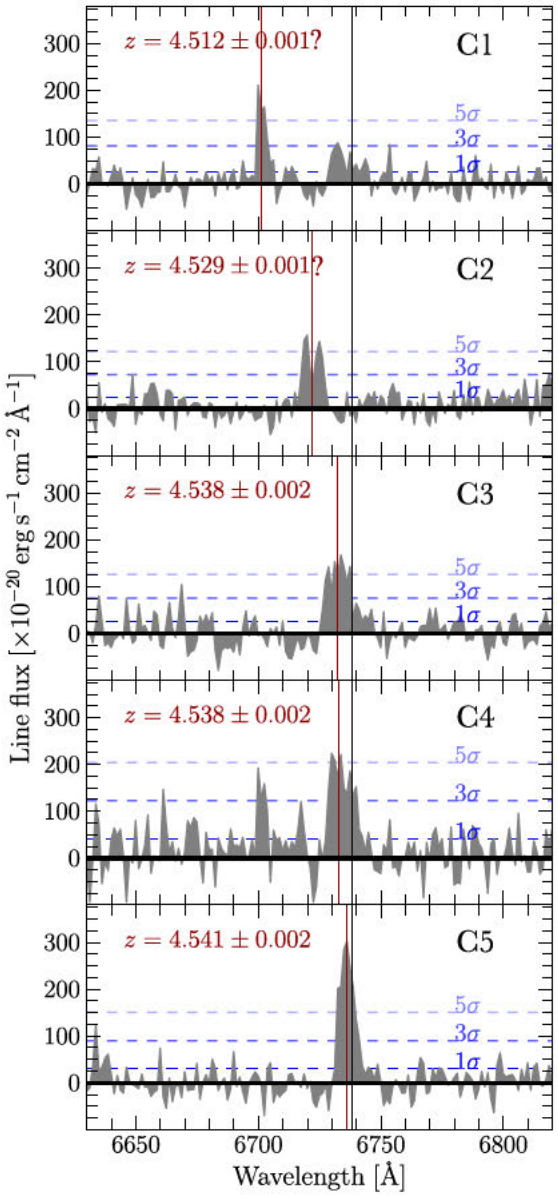

Figure 7. Optimally extracted 1D spectra of the five emitting sources in the vicinity of J1000+0234. The horizontal blue lines show the 1, 3, and 5× rms noise level. The vertical red lines show the (flux-weighted) central wavelength of the line profiles. The vertical black line marks the observed wavelength of Ly α line emission of J1000+0234. The photometric redshifts of C3, C4, and C5 allow us to identify the observed lines at ≈6735 Å as Ly α at $z \approx 4.5$. The properties of C1 and C2, and their UV counterparts, prevent a robust association between the observed ≈6710 Å lines with Ly α (see Section 4.3).

a comoving radius of 5 megaparsec (Mpc) and it is centred at only ≈500 comoving kpc away from J1000+0234. That extent matches the one expected for massive protogalaxy clusters (e.g. Chiang, Overzier & Gebhardt 2013, see our Section 5.3). At radii below 0.5 arcmin/1.2 comoving Mpc (cMpc), in particular, we derive an overdensity parameter of 6 ± 1. This analysis confirms the results based on the COSMOS2015 photometric redshift catalogue and the spectroscopic analysis presented in Smolčić et al. (2017a). Moreover, this result adds more evidence on the occurrence of LABs in galaxy overdensities at high redshifts (e.g. Matsuda et al. 2004; Alexander et al. 2016; Bădescu et al. 2017; Guaita et al. 2022).

5 DISCUSSION

In this section, we identify the possible ionization sources of the extended Ly α emission in J1000+0234. We also explore the Ly α and He II line profile across the nebula to infer the large-scale movements of the gas in the J1000+0234 system. Finally, we discuss the evolutionary path that J1000+0234 might follow, including the potential quenching of satellite galaxies and the origin of the red sequence of galaxies at $z \approx 2$.

5.1 Ionization source

Four main physical mechanisms have been proposed to explain the origin of circumgalactic Ly α emission: (a) recombination radiation following photoionization by UV photons (usually known as fluorescence; Hogan & Weymann 1987; Cantalupo et al. 2005); (b) UV photons from shock-heated gas powered by galactic outflows and/or relativistic jets (e.g. Taniguchi & Shioya 2000; Arrigoni Battaia et al. 2015); (c) resonant scattering of Ly α photons from an AGN and star formation (e.g. Villar-Martin, Binette & Fosbury 1996; Møller & Warren 1998; Dijkstra & Loeb 2009a; Hayes, Scarlata & Siana 2011; Cantalupo et al. 2014; Mas-Ribas et al. 2017; den Brok et al. 2020); and (d) cooling radiation from gas falling into dark matter halos (e.g. Fardal et al. 2001; Dijkstra & Loeb 2009a; Daddi et al. 2021). The latter is, however, unlikely to be the dominant process in J1000+0234, as there exist (at least) two strong sources of ionization within the nebula. First, there is a low-mass SFG (J1000+0234−South) with a UV luminosity that implies a SFR of $148 \pm 8\ M_\odot\ yr^{-1}$. Secondly, there is a dust-rich, rotating disc galaxy (J1000+0234−North) with a UV-based SFR of $52.6 \pm 8.5\ M_\odot\ yr^{-1}$, which represents ≈ 10 per cent of the total SFR (i.e. IR+UV SFR) of this massive SMG (Gómez-Guijarro et al. 2018).

Apart from star formation activity, two radio sources within the Ly α nebula might indicate AGN activity. The brightest radio source ($S_{3\,GHz} = 25 \pm 6$ μJy; Smolčić et al. 2017b) is centred at the locus of the SMG J1000+0234−North. We derive a monochromatic 1.4 GHz radio luminosity.[2] Of $L_{1.4\,GHz} = 5.2 \pm 1.2 \times 10^{24}\ W\ Hz^{-1}$ that is consistent with that of Type II AGNs at $z \approx 3.1$ (Ao et al. 2017; Marques-Chaves et al. 2019). The close-to-orthogonal position angles (PA) of the radio emission (33 ± 6 deg) and rotating disc of J1000+0234−North (145 ± 5 deg; Fraternali et al. 2021, see our Fig. 2) also hints at radio AGN activity, as the elongated radio emission suggests the presence of a jet moving perpendicular to the rotating [CII] disc. However, the FIR-to-1.4 GHz luminosity ratio $q_{FIR} = 1.9 \pm 0.1$ of J1000+0234−North is not significantly lower than the q_{FIR} value for SFGs at $z = 4.5$ of 2.1 ± 0.2 (Magnelli et al. 2015; Delhaize et al. 2017), suggesting that there is not a noticeably excess of radio emission in J1000+0234 due to AGN activity.

The faintest radio source within the Ly α nebula ($S_{3\,GHz} = 15 \pm 2$ μJy; Smolčić et al. 2017b) is not detected in existing ALMA imaging at 870 μm. It is located at 1.5 arcsec to the south-east of J1000+0234−North, along the direction of the potential radio jet coming out of the massive SMG. In this first scenario, the faint radio source might be tracing a radio jet/lobe. However, because there is faint UV emission at a projected distance < 0.5 arcsec from the centre of the faint radio source, it is also possible this is linked to a faint (and thereby undetected) SFG. Under this assumption, and using the rms noise level of the 870 μm map, we infer a 1σ upper limit of q_{FIR}

[2]Derived from the observed 3 GHz flux density and using the relation $S_\nu \propto \nu^{-\alpha}$ with $\alpha = 0.7$

Table 2. Ly α line emitters in the vicinity of J1000+0234.

Companion	RA (hh:mm:ss.sss)	Dec. (dd:mm:ss.ss)	$\lambda_{central}$ (Å)	z	Proj. area (arcsec^2 / kpc^2)	Iso flux ($\times 10^{-17}$erg s^{-1} cm^{-2})	Ly α luminosity ($\times$ 10^{42}erg s^{-1})
C1	10:00:54.158	02:34:22.32	6701.4	4.512 $\pm$ 0.001	7.2/315	0.74 $\pm$ 0.03	1.51 $\pm$ 0.07
C2[a]	10:00:55.679	02:34:13.23	6721.8	4.529 $\pm$ 0.001	10.5/460	0.83 $\pm$ 0.04	1.71 $\pm$ 0.10
C3	10:00:54.398	02:34:14.25	6732.5	4.538 $\pm$ 0.002	13.8/600	0.85 $\pm$ 0.04	1.76 $\pm$ 0.10
C4	10:00:54.105	02:34:20.55	6733.0	4.538 $\pm$ 0.002	25.2/1090	1.46 $\pm$ 0.05	3.03 $\pm$ 1.10
C5	10:00:54.841	02:34:27.49	6736.0	4.541 $\pm$ 0.002	10.7/462	1.76 $\pm$ 0.05	3.65 $\pm$ 0.10

[a]Assuming that C2 corresponds to the [OII] λ3727 doublet (see Section 4.3 for details), we compute $z = 0.803 \pm 0.001$, proj. area of 580 kpc^2, and [OII] luminosity of $2.36 \pm 0.11 \times 10^{40}$erg s^{-1}.

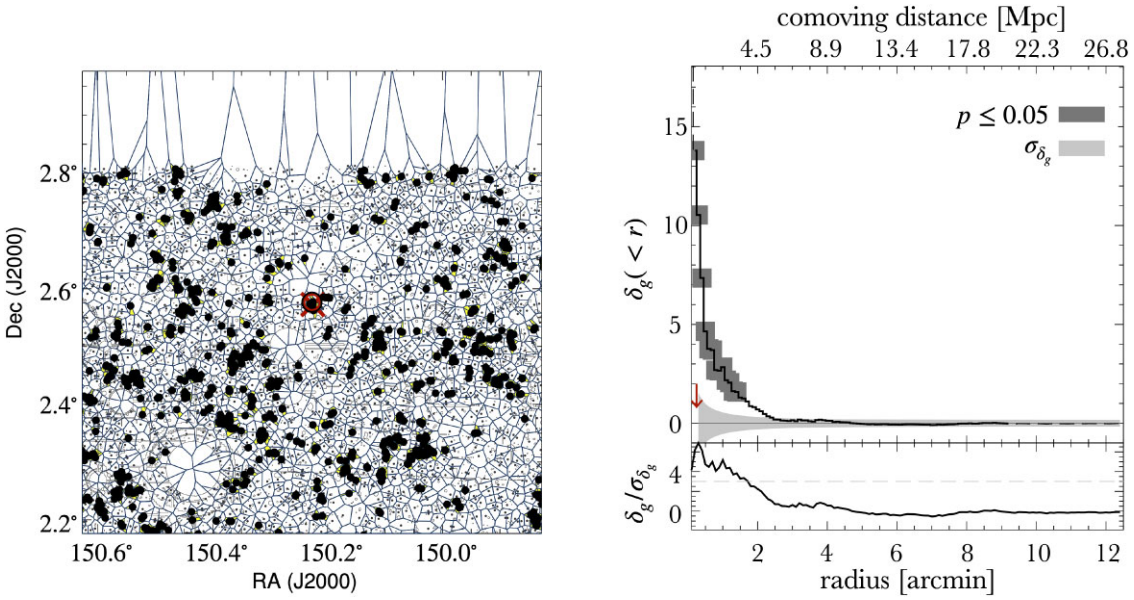

Figure 8. Left: Voronoi tessellation map around J1000+0234 (indicated by the red circle). Overdense VTA cells are shown in yellow. The overdensity centre is denoted by the red cross. Right: Galaxy overdensity as a function of distance to the overdensity centre. The grey region shows the error on the galaxy overdensity parameter. The grey squares mark robust overdensity values, for which the Poisson probability of observing more or an equal number of sources than expected from the background galaxy surface density is ≤ 5 per cent. The projected distance from the overdensity centre to J1000+0234 is indicated by the red downwards pointing arrow. The bottom panel presents the significance of the overdensity ($\delta_{gal}/\sigma_{\delta_{gal}}$) as a function of radius. The value of $\delta_{gal}/\sigma_{\delta_{gal}} = 3$ is indicated by the horizontal dashed line.

of 0.45[3] This value is five times lower than the q_{FIR} value for SFGs at $z = 4.5$. As suggested by Radcliffe et al. (2021), such a large radio excess with respect to the FIR-radio correlation of SFGs strongly suggests the presence of an AGN. We thus conclude that the faint radio source is likely another source of ionization of the Ly α nebula, either because this is a radio jet/lobe of the massive SMG or because this is tracing an AGN host galaxy that is not robustly detected in the UV nor FIR. Deeper multiwavelength, high-resolution data is needed to perform robust AGN diagnostics. For instance, current X-ray data only provides an upper limit for the X-ray luminosity of J1000+0234 of $10^{43.1}$erg s^{-1} (Smolčić et al. 2015), which is still significantly higher than the standard threshold to select X-ray AGN (10^{42}erg s^{-1}; Szokoly et al. 2004).

[3]The FIR luminosity is derived by adopting the rms noise level of the ALMA imaging as an upper limit of the 870 µm flux density. We then use the following approximation: $S^{SMG}_{870\,\mu m}/S^{r}_{870\,\mu m} \propto L^{SMG}_{FIR}/L^{r}_{FIR}$, where $S_{870\,\mu m}$ and L_{FIR} are the 870 µm flux density and FIR luminosity of the SMG and the compact radio source (r), respectively. Note that in this approximation, we assume that the radio source is linked to a dusty (yet faint and undetected) SFG whose dust spectral energy distribution has the same properties as that of the bright SMG.

5.1.1 *CIV/Ly α and He II/Ly α line ratios*

After identifying all the potential ionization sources in the field of the extended Ly α blob, we use the C IV and He II emission lines to better identify the origin and physical properties of the emitting gas.

In Fig. 9, we present the spatial distribution of the C IV/Ly α and He II/Ly α surface brightness (SB) ratios (upper panels) and their associated 1σ error (lower panels). These SB ratios are obtained as follows: (1) we obtain an optimally extracted SB map of Ly α emission using a spatial boxcar smoothing of 2 $\times$ 2 pixels, to match the smoothing applied to the C IV and He II SB maps (see Fig. 2), (2) we regrid the CIV and HeII SB maps to match both the pixel and sky coordinate system of the Ly α SB map, (3) we measure the rms noise level of the C IV and He II SB maps, (4) we replace each pixel without detected emission (i.e. SNR $<$ 3) in the optimally extracted C IV and He II SB maps with the 1σ noise value derived above, (5) we derive the C IV/Ly α and He II/Ly α line ratio on a pixel-by-pixel basis. Note that for the regions where CIV or

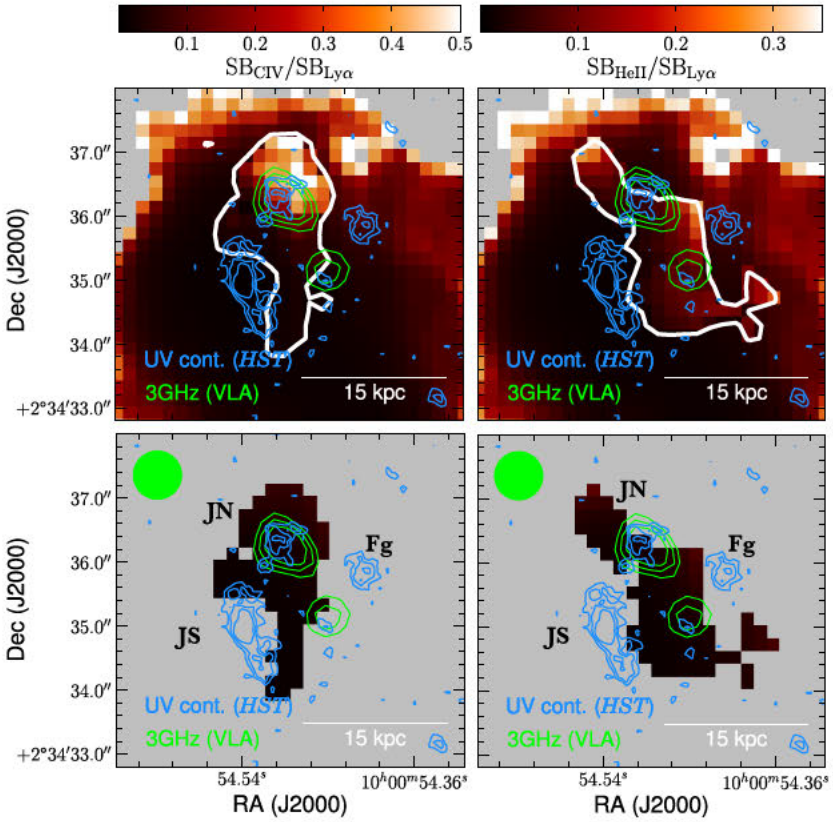

Figure 9. Upper panels: Spatial distributions of the C IV/Ly α and He II/Ly α SB ratios. The white contour delimits the region where C IV or He II is detected at a SNR > 3. The blue contours show the rest-frame UV continuum from the *HST*/F160W imaging and the lime contours display the VLA 3 GHz radio continuum emission (Smolčić et al. 2017b). Contour levels are the same as in Fig. 2. The pixel values outside the white contours are 1σ upper limits to the C IV/Ly α and He II/Ly α SB ratios (see the text for details). Lower panels: Spatial distribution of the 1σ uncertainties of the C IV/Ly α and He II/Ly α SB ratios. The VLA beam shape is shown in the upper-left corners. The regions with the highest C IV/Ly α and He II/Ly α ratios are located in the vicinity of J1000+0234−North (JN): a massive SMG, with signatures of AGN activity, that has a UV and 3 GHz radio counterpart. The lowest C IV/Ly α and He II/Ly α SB ratios, with a 1σ upper limit of ≈0.003, are located at the locus of J1000+0234−South (JS): a low-mass SFG that is bright in the UV and no signatures of AGN activity.

He II line emission is not detected, the C IV/Ly α and He II/Ly α values correspond to the line ratio 1σ upper limit. Finally, for the regions where the C IV/Ly α and He II/Ly α line ratios are derived, we estimate the associated 1σ error using the rms noise levels of the Ly α, C IV, and He II maps via standard error propagation on a pixel-by-pixel basis. Based on the spatial distribution of Ly α , C IV , and He II line emission, and their associated ratios (Figs 2 and 9), we identify three regions of interest within the Ly α nebula:

(i) First, we identify the area surrounding the massive, dusty, disc galaxy J1000+0234−North where CIV emission is maximal. This indicates the presence of a metal-enriched gaseous halo (e.g. Dopita et al. 2007; Reuland et al. 2007; Kolwa et al. 2019) around this source, which is consistent with J1000+0234−North being a massive, dust-rich, and likely a metal-enriched system (given the mass–metallicity relation; see Maiolino & Mannucci 2019, for a review). The detection of CIV also implies the presence of high-ionization radiation to triply ionize carbon, making this line a potential tracer of AGN activity (Baskin & Laor 2005; Mignoli et al. 2019). The average C IV/Ly α line ratio around the vicinity of the SMG is 0.40 ± 0.15. This is significantly higher than most of the line rations found in non-AGN LBG spectra (C IV/Ly $\alpha \leq 0.02$; Shapley et al. 2003), but more consistent with those values found in the LBG harbouring a narrow-line AGN (C IV/Ly $\alpha \approx 0.25$; Shapley et al. 2003) and local Seyfert galaxies (CIV/Ly $\alpha \approx 0.21$; Ferland & Osterbrock 1986). This finding thus strengthens the conclusion of our radio-FIR analysis that J1000+0234−North harbours an AGN.

(ii) Secondly, we recognize a more extended region where HeII emission is detected (Fig. 9). This is elongated along the relative position of the two radio continuum sources. The regions where the He II/Ly α ratio is maximal are placed on either side of J1000+0234−North, roughly along the direction of the bright radio source's major axis. Such a high line ratio in these regions, averaging He II/Ly $\alpha = 0.20 \pm 0.07$, is close to the recombination case for fully ionized hydrogen and helium (He II/Ly $\alpha = 0.3$ for Case B recombination Cantalupo et al. 2019). This suggests that, in the two nearby regions on either side of J1000+0234−North, the observed He II/Ly α line ratio is consistent with recombination processes, which take place after the exposure of the circumgalactic medium to the UV-flux from the AGN in J1000+0234−North. With a 1.4 GHz radio luminosity of $5.2 \pm 1.2 \times 10^{24}$ W Hz^{-1}, J1000+0234−North might harbour an AGN bolometric luminosity of the order of $10^{39.5}$ W Hz^{-1} (see fig. 3 of Sulentic, Zamfir & Marziani 2010) that is enough to produce an ionizing photon flux of $\phi \sim 10^{55}$ photons s^{-1} (see section 3.3.1 of Valentino et al. 2016). In the case of photoionization (see section 3.1 of Cantalupo 2017), such a photon flux implies a Ly α line luminosity of the order of 10^{44} erg s^{-1} that is comparable with the measured value. Additionally, the unobscured UV emission from J1000+0234−North might also account for a fraction of the total ionizing photons budget. Considering the

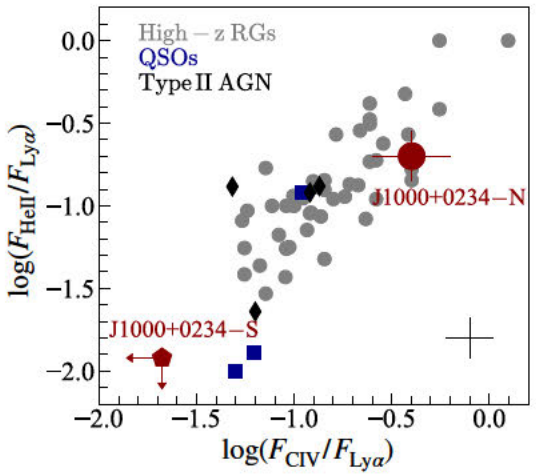

Figure 10. Ly α, He II, and C IV Line ratios of LABs previously associated with high-redshift radio galaxies (High-z RGs), QSOs, and Type II AGN (using data from Marino et al. 2019; Marques-Chaves et al. 2019; Wang et al. 2021; and references therein). The typical length of the error bars is shown in the bottom-right corner. The average line ratios around J1000+0234−North, the massive SMG with a potential AGN, are consistent with those observed in High-z RGs and Type II AGN. On the contrary, the 3σ upper limits to the average line ratios across the extent of J1000+0234−South, the low-mass starburst, suggest that a different mechanism is driving Ly α emission here.

relation $\mathrm{SFR}/\mathrm{M}_\odot\,\mathrm{yr}^{-1} = 0.62 \times L_{\mathrm{Ly}\alpha}/10^{42}\,\mathrm{erg\,s}^{-1}$ (Ao et al. 2017), the unobscured, UV-based SFR of J1000+0234−North (reported by Gómez-Guijarro et al. 2018) leads to a Ly α line luminosity of $33 \pm 5 \times 10^{42}\,\mathrm{erg\,s}^{-1}$ that is a factor 0.8 the measured value. Thus, an AGN and unobscured star formation activity in J1000+0234−North should produce enough ionizing photons to drive the Ly α nebula around the J1000+0234 system. Moreover, the tentative evidence of a radio lobe/jet, which matches the locus of bright He II and faint UV continuum emission (Fig. 2), hints at the possibility of jet–cloud interactions (e.g. Maxfield et al. 2002; Humphrey et al. 2006; Steinbring 2014) that could represent another ionization source in this region. In fact, the average C IV/Ly α and He II/Ly α line ratios in the vicinity of J1000+0234−North of 0.4 and 0.2, respectively, are consistent with those observed in Type II AGNs and high-redshift radio galaxies (Fig. 10).

(iii) Third, there is a region where Ly α emission is concentrically distributed around the low-mass SFG J1000+0234−South. This is also the area where Ly α emission peaks, which strongly suggests that Ly α emission is driven by photoionization (Villar-Martín et al. 2007) from the young starburst in J1000−0234−South, complementing the incident ionizing radiation from the nearby AGN in J1000+0234−North. The UV-based SFR of J1000+0234−South (reported by Gómez-Guijarro et al. 2018) implies Ly α line luminosity of $92 \pm 5 \times 10^{42}\,\mathrm{erg\,s}^{-1}$ that is two times the measured value, which suggests that the observed Ly α luminosity could also be explained by the intense star formation in J1000−0234−South. No CIV nor HeII line emission is detected across the UV extent of J1000+0234−South, which only allows us to estimate a 1σ upper limit of the C IV/Ly α and He II/Ly α line ratio of 0.007 and 0.004, respectively. Assuming that the starburst in J1000+0234−South does not produce a sufficiently hard radiation field, such low ratios suggest that the Lyα emitting gas around this low-mass galaxy does not receive enough incident flux above 4 Rydberg from the AGN in J1000+0234−North to double-ionize helium, either because of obscuration in that particular direction or because this part of the nebula is at a large distance from the AGN in J1000+0234−North. Indeed, the redshift from the HeII line of 4.545 ± 0.002, tracing the gas in the vicinity of the AGN, is mildly higher than the photometric redshift of J1000+0234−South (4.476 ± 0.025). However, as we discuss in the following section, due to the – likely high – peculiar velocities in this complex system, we cannot disentangle the physical separations (along the line of sight) of all the sources within the extended Ly α blob of J1000+0234. Alternatively, these rather low He II/Ly α ratio across and around J1000+0234−South can be a result of a broad density distribution of the circumgalactic gas in this region. Photoionization models for case B recombination from Cantalupo et al. (2019), that adopt a lognormal density distribution, suggest that large lognormal dispersions (σ_{gas}) of the gas density produce both smaller He II/Ly α line ratios and large Ly α SB values. Here, we observe $\mathrm{SB}_{\mathrm{Ly}\alpha} \gtrsim 10^{17}\,\mathrm{erg\,s}^{-1}\,\mathrm{cm}^{-2}\,\mathrm{arcsec}^{-2}$ and He II/Ly $\alpha < 0.004$ across and within the vicinity of the UV extent of J1000+0234−South, which imply σ_{gas} values above 2.0 (Cantalupo et al. 2019, see their fig. 8) that are comparable with those observed in the interstellar medium of galaxies.

In summary, based on their spatial distribution and potential ionization sources, we have identified three relevant zones within the Ly α nebula of J1000+0234. (1) A region around J1000+0234−North where CIV is present and He II/Ly α ratio is relatively high, this is likely where a Type II AGN is. (2) A region in the vicinity of the faint radio source with a relatively high He II/Ly α ratio that is possibly driven by jet–cloud interactions. (3) A region corresponding to the Ly α peak and J1000+0234−South. This is likely too distant and too dense for the AGN to double ionize He. Here, Ly α emission might be also due to the local (stellar) radiation field.

5.2 Ly α kinematics

The 1D spectrum of the J1000+0234 system (Fig. 3) reveals a wide, multipeaked, and asymmetric Ly α line profile that hints at complex and perturbed gas kinematics of a nebula or multiple structures with distinct peculiar velocities. To disentangle the contributions from these scenarios we combine information from our Ly α emission map with our HeII line detection.

At first glance, the integrated Ly α line profile of the J1000+0234 nebula (Fig. 3) resembles the expected profile of an expanding thin shell of neutral gas: one small blue-shifted wing, one narrow emission peak centred nearly at the systemic velocity, a red-shifted peak, and one extended red wing (e.g. Verhamme et al. 2006; Orsi et al. 2012). According to this model, the wide and asymmetric Ly α line profiles are a result of galactic-scale outflows driven by a central source (e.g. Taniguchi & Shioya 2000; Dawson et al. 2002; Dijkstra & Loeb 2009a). While photons experiencing multiple backscatterings produce an extended and redshifted wing, the external and expanding neutral HI gas along the line of sight absorbs the blue velocity component. This highly idealized model of a galaxy-scale expanding shell of neutral hydrogen around a central source seems, however, insufficient to explain the multicomponent and asymmetric morphology of the nebula and the multiple ionizing sources in the system (including AGN and star formation, see Section 5.1).

Another possible explanation for the asymmetric double-peaked Ly α line profile of J1000+0234 is the absorption of blue-shifted emission by the intervening intergalactic medium (e.g. Laursen et al. 2011). Hayes et al. (2021), in particular, find that the ratio of the blue/red wing intensity of a double-peaked Ly α line at $z = 4.5$ is only $\approx$0.1 (see their fig. 9). By extracting and inspecting the

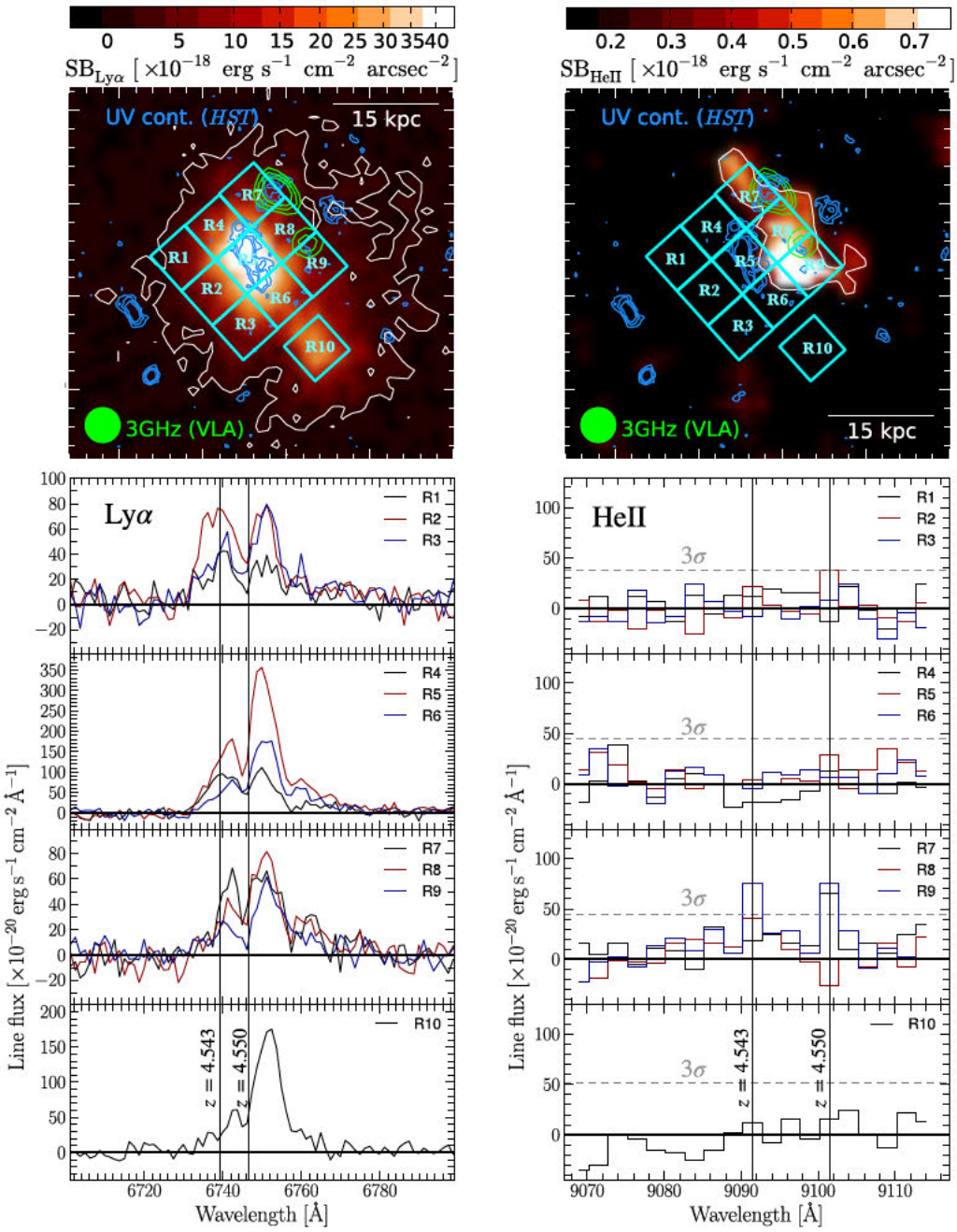

Figure 11. Upper panels: Optimally extracted SB maps of Ly α (left) and He II (right) emission in J1000+0234. The thin white contours indicate the SNR $= 3$ isophote. The blue contours show the rest-frame UV continuum from the *HST*/F160W imaging and the lime contours display the VLA 3 GHz radio continuum emission (Smolčić et al. 2017b). Contour levels are the same as in Fig. 2. The VLA beam shape is shown at the bottom-left corners. The cyan squares delimit the regions from which the 1D spectra shown in the lower panels are obtained. Lower panels: Ly α (left) and He II (right) line profiles across the extent of the J1000+0234 nebula. The He II spectra are averaged over a 3 Å-width bin. The horizontal, grey, and dashed lines illustrate the typical 3 $\times$ noise rms level of the 1D He II spectra. The black vertical lines show the expected central wavelength of the Ly α and He II lines of a source at $z = 4.543$ and $z = 4.550$, respectively. The double-peaked nature of the Ly α line persists across the brightest Ly α-emitting regions. The central wavelengths of the two peaks do not significantly vary across the 10 regions explored here. He II line emission is only detected in regions R7 and R9, corresponding to the locus of the bright SMG and the site of a possible radio jet (see details in Section 5.1). The marginal evidence of two peaks in the (non-resonant) He II line profile of regions R7–R9 suggests the presence of two different clouds along the line of sight.

Ly α line profile at different spatial locations of the J1000+0234 nebula (see the left-hand panels of Fig. 11), we find that the ratio of the blue/red wing intensity is larger than 0.1 and can be up to 1. Under this scenario, the low foreground absorption of the blue peak could indicate higher ionizing radiation from the J1000+0234 components that diminishes the neutral H I gas budget.

Alternatively, the two prominent peaks of the Ly α line profiles could correspond to two emitting clouds along the line of sight. We

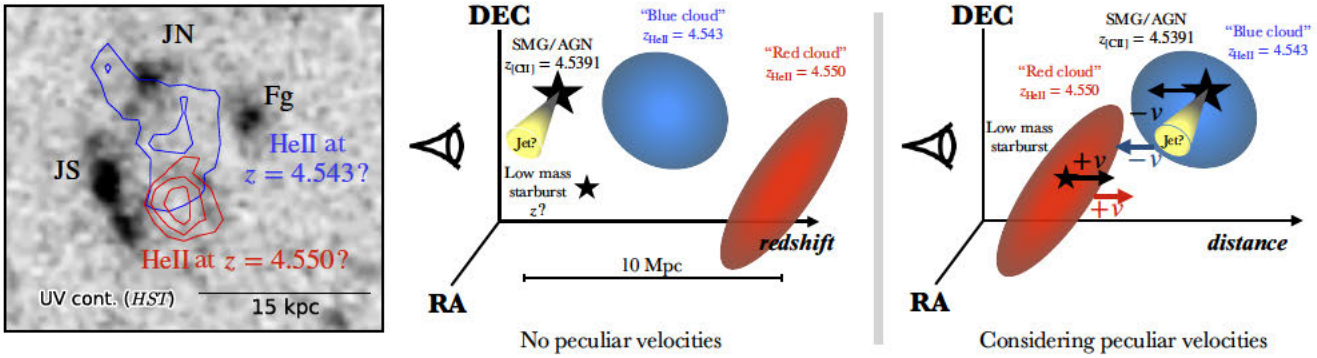

Figure 12. Left: Spatial distribution of redshifted/blueshifted HeII emission of J1000+0234 (blue and red contours, respectively) overlaid on the *HST*/F160W continuum image, which shows the rest-frame UV emission from the SMG J1000+0234−North (JN) and the low-mass starburst J1000+0234−South (JS). The prominent continuum source to the right of the J1000+0234 system is a foreground (Fg) galaxy (Capak et al. 2008). The red and blueshifted emission maps are obtained using the same 3D masks obtained during our source extraction procedure, but considering the channels lower/higher than 9095.0 Å to get optimally extracted NB images of the blue/redshifted He II emission. The contour levels are at 3, 4, 5, 6, and 7 times the noise rms level. The spatial (and spectral) offset (see Section 5.2) between the blueshifted and redshifted HeII emission of J1000+0234 suggests that these might represent two different clouds in the J1000+0234 system at $z = 4.543 \pm 0.002$ and $z = 4.550 \pm 0.002$. Middle: Cartoon illustrating the configuration along the line of sight of multiple components in the J1000+0234 system as inferred from their redshifts. If the effect of peculiar velocities is neglected, the redshift values would imply unrealistic comoving radial distances between the components on the order of Mpc (see Section 5.2 for details). Right: Assuming that the redshift values are also driven by peculiar velocities in the J1000+0234 system, that is in the centre of a galaxy overdensity, we propose that the two emitting clouds are on a collision course or receding from each other (after a passage) with a relative velocity of $\approx$400 km s^{-1}. In this cartoon, we illustrate the former scenario where the components are approaching one another before the passage. The lower [CII]-based redshift of J1000+0234 −North could be a result of a larger peculiar negative velocity along the line of sight. The direction and magnitude of the peculiar velocities of all the relevant components are represented by the black, blue, and red arrows.

evaluate this scenario by exploring the non-resonant He II emission extracting 1D spectra from the same regions employed to analyse the Ly α line profile across the nebula (see the right panels of Fig. 11). HeII emission is only detected in regions R7 and R9, i.e. around the SMG and the potential radio jet (see Section 5.1). Interestingly, the separation between the potential peaks of the He II line profile in R7/R9 is 10 Å, which corresponds to a velocity shift of $\approx$330 km s^{-1}. These values are similar to the velocity offset we observe in the double-peaked Ly α line profile across the entire nebula of $\approx$400 km s^{-1}. Hence, the peaks at 9091.5 and 9101.5 Å in the He II line profile of R7 and R9 might represent two different emitting clouds along the line of sight with redshifts 4.543 ± 0.002 and 4.550 ± 0.002. We note that the expected central wavelength of the Ly α line profile from those potentially distinct regions, shown in the lower-left panel of Fig. 11, does not agree with the observed central wavelength of the peaks, which could be explained by the resonant nature of the Ly α line emission that tends to be redshifted against the radial systemic velocity. Moreover, the scenario of two distinct clouds contributing to the Ly α nebula is reinforced by the significant spatial offset between the red and blueshifted He II emission of $\approx$6 kpc (see Fig. 12).

Under the scenario of two different line emitting clouds in the J1000+0234 system, the observed wavelength difference between the line peaks in the Ly α and He II line profiles could be a result of peculiar velocities and/or a different distance between them. If the velocity difference (δ_v) is solely due to the Hubble flow, the peaks shift would imply a physical distance of $\delta_v/H_0 \sim 5$ Mpc. This value is comparable to the extent of the galaxy overdensity within which the J1000+0234 system resides (see Section 4.3). We, therefore, consider this scenario unlikely. Instead, because J1000+0234 is a pair of likely interacting galaxies near the centre of a galaxy overdensity, where peculiar velocities are on the order of a few hundred km s^{-1}(e.g. Ceccarelli et al. 2005; Santucho, Ceccarelli & Lambas 2020), we would expect that the observed velocity offsets are largely driven by peculiar velocities. In this context, and based on the blue and red peak of the He II and Ly α lines, the apparent two emitting clouds in the J1000+0234 system are approaching one another (or receding from each other after a passage) with a relative velocity of $\approx$400 km s^{-1}. The relative motion between the multiple components in the J1000+0234 system could also explain the disagreement between the [CII]-derived redshift of J1000+0234−North (4.5391 ± 0.0004; Fraternali et al. 2021) and the redshift of the He II-emitting clouds ($z \approx 4.545$). A plausible scenario is that J1000+0234−North has a larger peculiar (negative) velocity – along the line of sight – than the blueshifted cloud within which the SMG/AGN is embedded (see the right-hand panel of Fig. 12). Since there are no spectroscopic redshift measurements of J1000+0234−South, we can only hypothesize that this low-mass starburst is embedded in the red-shifted cloud and is approaching (or receding from) the blueshifted cloud and the massive SMG J1000+0234−North.

5.3 The nature and fate of the complex J1000+0234 system

The J1000+0234 complex (J1000+0234−North and J1000+0234−South) and its companions reside in the central region of a large-scale overdensity of galaxies at $z = 4.5$, supporting the role of LABs as tracers of rich environments at high redshift (e.g. Matsuda et al. 2004; Alexander et al. 2016; Bădescu et al. 2017; Herenz et al. 2020; Guaita et al. 2022). In these overdense regions, the evolution of galaxies might be highly affected by environmental processes. Certainly, Gómez-Guijarro et al. (2018) proposed that J1000+0234−North and J1000−0234−South are undergoing a minor merger with a stellar mass ratio of 1:10, which might have contributed to triggering a Type II AGN and a vigorous starburst in J1000+0234−North – as suggested by numerical simulations (e.g. Hopkins et al. 2006). Merger activity could also explain the apparent elongation of both the rest-frame UV and Ly α emission around J1000+0234−South (Fig. 2), hinting at a tidal structure of young stars and gas resulting from the gravitational interaction.

While such a merger could be stripping gas from the minor companion J1000+0234−South, it is known that the mechanisms leading to stripping can briefly enhance star formation (e.g. Cortese, Catinella & Smith 2021, and references therein), consistent with the starburst nature of J1000+0234−South. As discussed in Section 5.1, vigorous star formation activity might be the dominant ionization source of Ly α emission around J1000+0234−South, while AGN activity and dust-unobscured star formation are the potential main drivers of extended Ly α emission around J1000+0234−North. Our kinematical analysis suggests the presence of two He II emitting clouds along the line of sight with a relative velocity of 400 km s^{-1}, consistent with the scenario in which J1000+0234 is an interacting system whose components are on a collision course or receding from each other (after a passage). Interestingly, despite the indications of galaxy interactions in this system, the SMG J1000+0234−North preserves a rotationally supported gas disk, suggesting that any previous merging activity (that triggered the AGN and the starburst phase in the J1000+0234 system) involved low-mass companions that did not disrupt the disk. This scenario has been proposed for the SMG W0410-0913 that also harbours a rotationally-supported gas disk and resides in an overdense environment at $z \approx 3.6$ (Ginolfi et al. 2022). The results presented here (and in Ginolfi et al. 2022) agree with expectations from numerical simulations indicating that, rather than major mergers, smooth accretion from cosmological filaments and minor mergers are the dominant mechanisms regulating the growth of high-redshift galaxies in overdense environments (Romano-Díaz et al. 2014). Also, the observed properties of J1000+0234 seem to agree with numerical simulations predicting that merging activity does not necessarily disrupt disks, particularly in gas-rich systems like J1000+0234 (Schinnerer et al. 2008) where even the residual gas from major mergers may reform a disk (e.g. Springel & Hernquist 2005; Romano-Díaz et al. 2011; Martin et al. 2018; Peschken, Łokas & Athanassoula 2020) – albeit other physical conditions like the orbital configuration of the merging system (Zeng, Wang & Gao 2021) and the time after the merger may be at play here as well.

The evolutionary path that the system J1000+0234 will follow can be discussed in terms of cluster formation and the assembly of local elliptical galaxies. We first use the predictions from cosmological simulations in Chiang et al. (2013) to verify if J1000+0234 matches the expected observational signatures of galaxy proto-clusters. Based on the results shown in Fig. 8, the overdensity around J1000+0234 extends out to a 5cMpc radius (10cMpc diameter) where $\delta_g \approx 0.5$. Comparing with the results from Chiang et al. (2013) for a (15 cMpc)^3 volume, that is the one that resembles the most to our observations, we find that the overdensity around J1000+0234 at $z = 4.5$ has a low probability (<20%) to evolve into a galaxy cluster with a total mass of $\approx 10^{14}$ M$_\odot$ at $z = 0$. In that event, the J1000+0234 system would be consistent with the proposed evolutionary link between $z > 3$ SMGs and their descendant, massive elliptical galaxies at $z = 0$ (Geach et al. 2005; Toft et al. 2014; Stach et al. 2021) that preferentially reside at the centre of galaxy clusters. Such a scenario involves the abrupt cessation of star formation in $z > 3$ dusty starbursts (Jones et al. 2017) that subsequently merge with *quenched* satellite galaxies (e.g. Davé, Rafieferantsoa & Thompson 2017). As previously discussed by Gómez-Guijarro et al. (2018) and Fraternali et al. (2021), there exists indirect evidence suggesting a possible evolution of J1000+0234 into a local early-type galaxy. First, the expected growth in mass and size of the SMG J1000+0234−North, including the contribution of minor mergers, broadly agrees with the properties of the compact quiescent galaxies at $z \approx 2$ (Gómez-Guijarro et al. 2018) that are the progenitors of local massive ellipticals. Second, the inner potential well of the SMG J1000+0234−North, probed by the [CII] kinematics, is comparable with that of the most massive early-type galaxies in the local universe (Fraternali et al. 2021), providing dynamical evidence of the evolutionary link between the J1000+0234 system and local ellipticals.

While the observational results presented here suggest that J1000+0234 reside at the centre of a potential proto-cluster, the mechanisms that can suppress star formation in the central SMG J1000+0234−North remain unclear. A plausible scenario might involve 'mass quenching'. Galaxies with stellar masses a factor of ∼2 larger than J1000+0234−North (i.e. $M_\star \sim 10^{10.5}$ M$_\odot$, with dark matter haloes $\sim 10^{12}$ M$_\odot$) are expected to form a hot gas corona that can shut off the gas supply from the cosmic web and prevent the cooling of gas (Gabor et al. 2010, and references therein). The activity of an AGN, like the one inferred for J1000+0234−North, can act as an additional heating source (e.g. Croton et al. 2006), suppressing the formation of stars in such massive galaxies.

6 CONCLUSIONS

We use MUSE observations to characterize extended Ly α, C IV, and He II emission around J1000+0234; a pair of galaxies at $z = 4.5$ in the COSMOS field. J1000+0234−North is a massive SMG ($\log(M_\star/M_\odot) = 10.1 \pm 0.1$) exhibiting a rotating [CII] disc with SFR $= 500^{+1200}_{-320}$ $M_\odot$ yr^{-1}(Gómez-Guijarro et al. 2018; Fraternali et al. 2021), while J1000+0234−South is a UV-bright, low-mass SFG ($\log(M_\star/M_\odot) = 9.2 \pm 0.1$) with SFR $= 148 \pm 8$ $M_\odot$ yr^{-1}(Gómez-Guijarro et al. 2018). By combining MUSE observations with existing ALMA and *HST* data, we find the following:

(i) We detect Ly α emission that peaks at the locus of J1000+0234−South and extends over a projected area of 1853 kpc^2, with a maximum linear projected size of ≈43 kpc (Fig. 2). Based (optimally extracted) flux of $F^{\rm obs}_{{\rm Ly}\,\alpha} = (19.79 \pm 0.15) \times 10^{-17}$erg s^{-1} cm^{-2}, we compute a total line luminosity of $L^{\rm obs}_{{\rm Ly}\,\alpha} = (40.17 \pm 0.31) \times 10^{42}$erg s^{-1}. J1000+0234 is among the most compact and least luminous high-redshift Ly α nebulae (see Fig. 4).

(ii) HeII line emission is also detected around J1000+0234−North (Fig. 2). This emission, extending out to a projected area of 3.7 arcsec^2 ≈ 159 kpc^2, reaches a maximum near the locus of a faint radio source at 1.″5 to the South-West of J1000+0234−North (likely a radio jet). With a flux of $F^{\rm obs}_{\rm HeII} = (0.27 \pm 0.03) \times 10^{-17}$ erg s^{-1} cm^{-2}, we compute a to total line luminosity of $L_{\rm He\,II} = (0.57 \pm 0.06) \times 10^{42}$ erg s^{-1}.

(iii) We detect CIV line emission around J1000+0234−North that extends out to a projected area of 3.7 arcsec^2 ≈ 159 kpc^2 (Fig. 2). The measured flux of $F^{\rm obs}_{\rm CIV} = (0.37 \pm 0.03) \times 10^{-17}$ erg s^{-1} cm^{-2} leads to a total line luminosities of $L_{\rm C\,IV} = (0.76 \pm 0.07) \times 10^{42}$ erg s^{-1}.

(iv) We detect three Ly α emitters (C3, C4, C5) spanning over a redshift bin $\Delta z \leq 0.007$ (i.e. $\lesssim 380$ km s^{-1}) located at $\lesssim 140$ kpc from J1000+0234 (Fig. 6). These companions have a projected area ranging from 460 to 1090 kpc^2 and Ly α line luminosities of $1.8-3.6 \times 10^{42}$ erg s^{-1}. We identify a galaxy overdensity that is centred at only ≈500 comoving kpc away from the J1000+0234 system. We estimate an overdensity parameter (δ_g) of 6 ± 1 at a comoving radius of 1.2 Mpc. This result supports earlier indications that J1000+0234 lies near the centre of a Mpc-scale galaxy overdensity at $z = 4.5$ (Smolčić et al. 2017a).

(v) The C IV/Ly α and He II/Ly α Line ratios are maximal in the vicinity of J1000+0234−North (Fig. 9). These line ratios (≈0.2−0.4) are consistent with those observed in Type II AGN and high-redshift radio galaxies (Shapley et al. 2003; Marques-Chaves

et al. 2019). Here, Ly α emission might be driven by the AGN and associated jet in J1000+0234−North.

(vi) At the locus of J1000+0234−South, where Ly α emission peaks but no HeII nor CIV emission is detected (Figs 2 and 9), the C IV/Ly α and He II/Ly α line ratios are smaller than 0.007 and 0.004, respectively. These low line ratios hint at the possibility that the gas around J1000+0234−South does not receive enough incident flux from the AGN. Here, Ly α emission might be driven by the starburst in J1000+0234−South.

(vii) There is marginal evidence for two HeII-emitting clouds separated by 10 Å and 6 kpc (projected on the sky plane). This suggests that the velocity structure of this LAB is the result of two overlapping haloes. The two Ly α peaks might correspond to two emitting clouds in the J1000+0234 system approaching one another (or receding from each other after a passage) with a relative velocity of $\approx$400 km s^{-1}.

This study strengthens the role of LABs as observational signatures of galaxy overdensities at high redshifts, within which galaxy mergers can trigger intense star formation and AGN episodes in a central, dust-enshrouded massive galaxy that preserves a rotationally supported gas disc. The clustering around J1000+0234 also hints at the proposed evolutionary link between SMGs in rich environments and local elliptical galaxies that reside at the centre of galaxy clusters. Moreover, this work is an instructive example of how spatially resolved observations of He II and C IV line emission are key to unveiling the driving mechanism of high-redshift LABs, particularly those associated with the core of galaxy overdensities where total line ratios can be strongly affected by blending. This study also showcases the benefits of using the HeII line emission to study the gas kinematics within LABs, because observations of the non-resonant Ly α line convey more uncertainties to the already complex configuration of peculiar velocities in the centre of galaxy overdensities. In this context, observations with the *James Webb Space Telescope* will be necessary to map the kinematical structure of $z \approx 4$ protocluster of galaxies using, for example, H α and H β, which will also serve to unveil the relative contribution of AGN, star formation, and cooling radiation to the origin of LABs.

ACKNOWLEDGEMENTS

We thank the reviewer for their constructive comments and suggestions. EFJA gratefully acknowledges the support from the NRAO staff that made remote working feasible during the COVID-19 pandemic. EFJA, BM, and ERD acknowledge support of the Collaborative Research Center 956, subproject A1 and C4, funded by the Deutsche Forschungsgemeinschaft (DFG). SC gratefully acknowledges support from the European Research Council (ERC) under the European Union's Horizon 2020 research and innovation programme grant agreement no. 864361. The Cosmic Dawn Center (DAWN) is funded by the Danish National Research Foundation under grant no. 140. This study is based on observations collected at the European Southern Observatory under ESO programmes 0102.A-0448 and 0103.A-0272.

DATA AVAILABILITY

The data underlying this article can be accessed from the ESO Archive Science portal (http://archive.eso.org/scienceportal/home) under the programmes 0102.A-0448 and 0103.A-0272 with the object identifier 'COSMOSz4' and 'J1000+0234'. The derived data generated in this research will be shared on reasonable request to the corresponding author.

REFERENCES

Alexander D. M. et al., 2016, MNRAS, 461, 2944
Ao Y. et al., 2017, ApJ, 850, 178
Ao Y. et al., 2020, Nature Astron., 4, 670
Arrigoni Battaia F., Yang Y., Hennawi J. F., Prochaska J. X., Matsuda Y., Yamada T., Hayashino T., 2015, ApJ, 804, 26
Bădescu T., Yang Y., Bertoldi F., Zabludoff A., Karim A., Magnelli B., 2017, ApJ, 845, 172
Baskin A., Laor A., 2005, MNRAS, 356, 1029
Behrens C., Braun H., 2014, A&A, 572, A74
Borisova E. et al., 2016, ApJ, 831, 39
Bridge C. R. et al., 2013, ApJ, 769, 91
Cai Z. et al., 2017, ApJ, 837, 71
Caminha G. B. et al., 2016, A&A, 595, A100
Cantalupo S., 2017, Gas Accretion onto Galaxies, Astrophysics and Space Science Library. Springer, Switzerland, p. 195
Cantalupo S., Porciani C., Lilly S. J., Miniati F., 2005, ApJ, 628, 61
Cantalupo S., Arrigoni-Battaia F., Prochaska J. X., Hennawi J. F., Madau P., 2014, Nature, 506, 63
Cantalupo S. et al., 2019, MNRAS, 483, 5188
Capak P. et al., 2008, ApJ, 681, L53
Ceccarelli M. L., Valotto C., Lambas D. G., Padilla N., Giovanelli R., Haynes M., 2005, ApJ, 622, 853
Chiang Y.-K., Overzier R., Gebhardt K., 2013, ApJ, 779, 127
Cortese L., Catinella B., Smith R., 2021, PASA, 38, e035
Croton D. J. et al., 2006, MNRAS, 365, 11
Daddi E. et al., 2021, A&A, 649, A78
Davé R., Rafieferantsoa M. H., Thompson R. J., 2017, MNRAS, 471, 1671
Dawson S., Spinrad H., Stern D., Dey A., van Breugel W., de Vries W., Reuland M., 2002, ApJ, 570, 92
Delhaize J. et al., 2017, A&A, 602, A4
den Brok J. S. et al., 2020, MNRAS, 495, 1874
Dey A. et al., 2005, ApJ, 629, 654
Dijkstra M., Loeb A., 2009a, MNRAS, 396, 377
Dijkstra M., Loeb A., 2009b, MNRAS, 400, 1109
Dopita M. A. et al., 2007, Ap&SS, 311, 305
Erb D. K., Bogosavljević M., Steidel C. C., 2011, ApJ, 740, L31
Fardal M. A., Katz N., Gardner J. P., Hernquist L., Weinberg D. H., Dave R., 2001, ApJ, 562, 605
Farina E. P. et al., 2017, ApJ, 848, 78
Faucher-Giguère C.-A., Hopkins P. F., Kereš D., Muratov A. L., Quataert E., Murray N., 2015, MNRAS, 449, 987
Ferland G. J., Osterbrock D. E., 1986, ApJ, 300, 658
Fraternali F., Karim A., Magnelli B., Gómez-Guijarro C., Jiménez-Andrade E. F., Posses A. C., 2021, A&A, 647, A194
Gabor J. M., Davé R., Finlator K., Oppenheimer B. D., 2010, MNRAS, 407, 749
Geach J. E. et al., 2005, MNRAS, 363, 1398
Geach J. E. et al., 2014, ApJ, 793, 22
Geach J. E. et al., 2016, ApJ, 832, 37
Ginolfi M., Maiolino R., Carniani S., Arrigoni Battaia F., Cantalupo S., Schneider R., 2018, MNRAS, 476, 2421
Ginolfi M. et al., 2022, Nature Commun., 13, 4574
Glazebrook K. et al., 2017, Nature, 544, 71
Gobat R. et al., 2012, ApJ, 759, L44
Gómez-Guijarro C. et al., 2018, ApJ, 856, 121
Guaita L. et al., 2022, A&A, 660, A137
Gurung-Lopez S., Gronke M., Saito S., Bonoli S., Orsi A. A., 2021, MNRAS, 510, 4525
Hayes M., Scarlata C., Siana B., 2011, Nature, 476, 304
Hayes M. J., Runnholm A., Gronke M., Scarlata C., 2021, ApJ, 908, 36
Hennawi J. F., Prochaska J. X., Cantalupo S., Arrigoni-Battaia F., 2015, Science, 348, 779

Herenz E. C., Hayes M., Scarlata C., 2020, A&A, 642, A55
Hine N. K. et al., 2016, MNRAS, 460, 4075
Hogan C. J., Weymann R. J., 1987, MNRAS, 225, 1P
Hopkins P. F., Hernquist L., Cox T. J., Matteo T. D., Robertson B., Springel V., 2006, ApJS, 163, 1
Humphrey A., Villar-Martín M., Fosbury R., Vernet J., di Serego Alighieri S., 2006, MNRAS, 369, 1103
Humphrey A., Villar-Martín M., Binette L., Raj R., 2019, A&A, 621, A10
Jones G. C. et al., 2017, ApJ, 850, 180
Kennicutt J. R. C., 1998, ARA&A, 36, 189
Kolwa S. et al., 2019, A&A, 625, A102
Laigle C. et al., 2016, ApJSS, 224, 24
Lake E., Zheng Z., Cen R., Sadoun R., Momose R., Ouchi M., 2015, ApJ, 806, 46
Laursen P., Sommer-Larsen J., Razoumov A. O., 2011, ApJ, 728, 52
Leclercq F. et al., 2017, A&A, 608, A8
Leclercq F. et al., 2020, A&A, 635, A82
Li Q. et al., 2021, ApJ, 922, 236
McCarthy P. J., Spinrad H., Djorgovski S., Strauss M. A., van Breugel W., Liebert J., 1987, ApJ, 319, L39
Magnelli B. et al., 2015, A&A, 573, A45
Maiolino R., Mannucci F., 2019, A&AR, 27, 3
Marino R. A. et al., 2019, ApJ, 880, 47
Marques-Chaves R. et al., 2019, A&A, 629, A23
Martin G., Kaviraj S., Devriendt J. E. G., Dubois Y., Pichon C., 2018, MNRAS, 480, 2266
Mas-Ribas L., Dijkstra M., Hennawi J. F., Trenti M., Momose R., Ouchi M., 2017, ApJ, 841, 19
Matsuda Y. et al., 2004, AJ, 128, 569
Matsuda Y. et al., 2012, MNRAS, 425, 878
Maxfield L., Spinrad H., Stern D., Dey A., Dickinson M., 2002, AJ, 123, 2321
Mignoli M. et al., 2019, A&A, 626, A9
Møller P., Warren S. J., 1998, MNRAS, 299, 661
Momose R. et al., 2016, MNRAS, 457, 2318
Orsi A., Lacey C. G., Baugh C. M., 2012, MNRAS, 425, 87
Ouchi M., Ono Y., Shibuya T., 2020, ARA&A, 58, 617
Peschken N., Łokas E. L., Athanassoula E., 2020, MNRAS, 493, 1375
Prescott M. K. M., Dey A., Jannuzi B. T., 2009, ApJ, 702, 554
Radcliffe J. F., Barthel P. D., Thomson A. P., Garrett M. A., Beswick R. J., Muxlow T. W. B., 2021, A&A, 649, A27
Reuland M. et al., 2007, AJ, 133, 2607
Romano-Díaz E., Choi J.-H., Shlosman I., Trenti M., 2011, ApJ, 738, L19
Romano-Díaz E., Shlosman I., Choi J.-H., Sadoun R., 2014, ApJ, 790, L32
Sadoun R., Romano-Díaz E., Shlosman I., Zheng Z., 2019, MNRAS, 484, 4601
Sanderson K. N., Prescott M. K. M., Christensen L., Fynbo J., Møller P., 2021, ApJ, 923, 252
Santucho M. V., Ceccarelli M. L., Lambas D. G., 2020, A&A, 642, A131
Schinnerer E. et al., 2008, ApJ, 689, L5
Schreiber C. et al., 2015, A&A, 575, A74
Scott K. S. et al., 2008, MNRAS, 385, 2225
Shapley A. E., Steidel C. C., Pettini M., Adelberger K. L., 2003, ApJ, 588, 65
Shibuya T. et al., 2018, PASJ, 70, S14
Smolčić V. et al., 2015, A&A, 576, A127
Smolčić V. et al., 2017a, A&A, 597, A4
Smolčić V. et al., 2017b, A&A, 602, A1
Solimano M. et al., 2022, ApJ, 935, 17
Song H., Seon K.-I., Hwang H. S., 2020, ApJ, 901, 41
Springel V., Hernquist L., 2005, ApJ, 622, L9
Stach S. M. et al., 2021, MNRAS, 504, 172
Steidel C. C., Adelberger K. L., Shapley A. E., Pettini M., Dickinson M., Giavalisco M., 2000, ApJ, 532, 170
Steidel C. C., Bogosavljević M., Shapley A. E., Kollmeier J. A., Reddy N. A., Erb D. K., Pettini M., 2011, ApJ, 736, 160
Steinbring E., 2014, AJ, 148, 10
Sulentic J., Zamfir S., Marziani P., 2010, in Maraschi L., Ghisellini G., Della Ceca R., Tavecchio F., eds, ASP Conf. Ser. Vol. 427, Accretion and Ejection in AGN: a Global View. Astron. Soc. Pac., San Francisco, p. 371
Swinbank A. M. et al., 2015, MNRAS, 449, 1298
Szokoly G. P. et al., 2004, ApJS, 155, 271
Taniguchi Y., Shioya Y., 2000, ApJ, 532, L13
Toft S. et al., 2014, ApJ, 782, 68
Travascio A. et al., 2020, A&A, 635, A157
Valentino F. et al., 2016, ApJ, 829, 53
Verhamme A., Schaerer D., Maselli A., 2006, A&A, 460, 397
Villar-Martin M., Binette L., Fosbury R. A. E., 1996, A&A, 312, 751
Villar-Martín M., Tadhunter C., Clark N., 1997, A&A, 323, 21
Villar-Martín M., Humphrey A., De Breuck C., Fosbury R., Binette L., Vernet J., 2007, MNRAS, 375, 1299
Wang W., Wylezalek D., De Breuck C., Vernet J., Humphrey A., Villar Martín M., Lehnert M. D., Kolwa S., 2021, A&A, 654, A88
Weaver J. R. et al., 2022, ApJSS, 258, 11
Weilbacher P. M., Streicher O., Urrutia T., Pécontal-Rousset A., Jarno A., Bacon R., 2014, in Manset N., Forshay P., eds, ASP Conf. Ser. Vol. 485, Astronomical Data Analysis Software and Systems XXIII. Astron. Soc. Pac., San Francisco, p. 451
Wilson G. W. et al., 2008, MNRAS, 386, 807
Wisotzki L. et al., 2016, A&A, 587, A98
Wisotzki L. et al., 2018, Nature, 562, 229
Xue R. et al., 2017, ApJ, 837, 172
Zeng G., Wang L., Gao L., 2021, MNRAS, 507, 3301
Zheng Z., Cen R., Trac H., Miralda-Escudé J., 2010, ApJ, 716, 574

This paper has been typeset from a TEX/LATEX file prepared by the author.